

國立交通大學

機械工程學系

碩士論文

觀測器基礎純加速規平面式慣性量測單元

Observer-Based Planar Gyro-Free Inertial Measurement
Unit

研究生：陳奕龍

指導教授：陳宗麟 博士

中華民國九十四年七月

觀測器基礎純加速規平面式慣性量測單元

Observer-Based Planar Gyro-Free Inertial Measurement Unit

研究生：陳奕龍

Student: Yi-Long Chen

指導教授：陳宗麟

Advisor: Dr. Tony Chen

國立交通大學

機械工程學系



Submitted to Department of Mechanical Engineering

College of Engineering

National Chiao Tung University

in partial Fulfillment of the Requirement

for the Degree of

Master of Science

in

Mechanical Engineering

July 2005

Hsinchu, Taiwan, Republic of China

中華民國九十四年七月

觀測器基礎純加速規平面式慣性量測單元

研究生：陳奕龍

指導教授：陳宗麟博士

國立交通大學機械工程學系

摘要

本論文主要是由多顆加速規量測空間中運動物體之角速度及線性加速度，此一做法統稱之為慣性量測單元。



傳統上慣性標測單元由陀螺儀量測角加速度及加速規量測線性加速度，則在求得空間中物體位置及姿態時須經過兩次積分，此一作法會造成嚴重之誤差累積。於是 20 年前發展藉由加速規擺放位置不同求得角加速度，此種做法降低了慣性量測單元生產成本，但未能解決兩次積分造成的嚴重誤差。無論使用陀螺儀或是加速規得到角加速度，都是事先製作好再擺放至慣性量測單元上，這樣在擺放時會造成另外的誤差產生。

本論文的做法是利用微機電製程在同一平面上同時製作九顆加速規，不但降低成本也解決擺放時造成的誤差。並且，利用觀測器之觀念直接求得物體之角速度，在求得物體姿態上減低了一次積分的動作，對積分誤差之累積改善了不少。並在論文的最後並以實驗佐證此一構想是可行的。

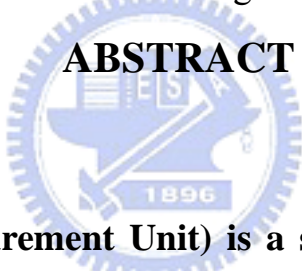
Observer-Based Planar Gyro-Free Inertial Measurement Unit

Student: Yi-Long Chen

Advisor: Dr. Tony Chen

Department of Mechanical Engineering
National Chiao Tung University

ABSTRACT



IMU (Inertial Measurement Unit) is a sensor unit that can provide the position information (angular acceleration, angular velocity, linear acceleration and etc.) for an object in motion. Typical IMU uses three gyroscopes to sense the angular velocity and three linear accelerometers to sense the linear acceleration. The output from 3 gyroscopes undergoes integral operation to obtain 3 rotation angles; and the output from 3 linear accelerometers undergoes integration operation twice to obtain 3 coordinates for location. Another approach is named “Gyro-free IMU”, which only the linear accelerometers are utilized. The output of Gyro-free IMU consists of 3 angular accelerations and 3 linear accelerations, which need 2 consecutive integral operations to obtain rotation angles and 2 consecutive integral operations to obtain 3 location

coordinates in space. The integral operation will result in the error accumulation and should be avoided or minimized, if possible.

Due to the convergence properties of Gyro-free IMU, the accelerometers utilized must be deployed in a 3D location manner. As a consequence, the accelerometers must be fabricated in prior to the IMU and then mounted on the various locations of IMU. This approach inevitably results in misalignment error for the placement of accelerometers.

In correspondence to the existing problems mentioned above, we proposed the brand new design “observer-base planar Gyro-Free IMU” to solve those problems.



ACKNOWLEDGEMENT

本論文能夠順利完成，首先要感謝指導恩師 陳宗麟老師這兩年來悉心的督促及指導。在與恩師的互動中，不但學習到專業的知識與進行研究所需的態度，也瞭解到如何掌握問題核心與審慎分析的能力。在此獻上誠摯的謝意與敬意。

感謝博士班紀建宇學長，在課業上與生活上都不厭其煩地給予提攜與幫助，尤其是研究過程中，對我的盡心指導，給了我許多寶貴的意見使得論文的研究更加完整。邱仕釗同學、黃建評同學、郭威廷同學及實驗室的學弟，在課業與研究上互相打氣、彼此砥礪，使我獲益良多。

最後要感謝父親陳文成、母親李新美兩人無盡的愛心與細心的栽培，讓我在生活上與精神上都能夠獲得充分的支持與協助。也要感謝弟弟陳奕志及大學的同窗好友的幫助與鼓勵，才能在無後顧之憂的情況下順利完成學業。

對於我最親愛的家人和所有關心我的朋友們，僅以本論文獻給你們，再次地感謝你們。

TABLE OF CONTENTS

摘要	II
ABSTRACT.....	III
ACKNOWLEDGEMENT	V
TABLE OF CONTENTS.....	VI
LIST OF TABLE	IX
LIST OF FIGURES	X
CHAPTER 1 INTRODUCTION.....	1
CHAPTER 2 THEORY AND ALGORITHM	5
2.1 Motion of Rigid Body in Space	5
2.2 Location of accelerometers and Dynamic system	7
2.3 Kalman filter.....	13
2.3.1 The Extended Kalman Filter.....	13
State prediction	15
Measurement prediction	15
Filter gain	16

Update.....	16
2.3.2 The Iterated Extended Kalman Filter	18
Overview of the Iteration Sequence	18
2.4 Orthogonal Transfer Matrix	19
2.5 Flow chart	22
CHAPTER 3 SIMULATION AND PRELIMINARY TEST	23
3.1 Test structure	23
3.2 Generate Motion.....	24
3.3 One Axis Tested.....	25
3.4 Simulation and Resolution.....	27
Resolution.....	31
CHAPTER 4 TEST OF THE IMU DESIGN.....	33
4.1 Experimental procedure	33
Basic procedure of experiment.....	34
Route of motion.....	36
Low-pass analog amplifier (single pole)	36
Butterworth filter	37
4.2 Z-axis rotation with biaxial linear acceleration.....	38

4.3 Z-axis rotation with biaxial linear acceleration and non-zero initial condition	49
4.4 Y-axis rotation with biaxial linear acceleration	55
4.5 Discussion	61
Linear vibrations of the optical table.....	61
Rotational vibration of the optical table.....	64
DC-drift or other noise.....	65
CHAPTER 5 CONCLUSION AND FUTURE WORKS	69
5.1 Conclusion.....	69
5.2 Future works.....	70
References.....	71



LIST OF TABLE

Table 1	Location and Sensing direction of the accelerometers	10
Table 2	Flow chart of first order Extended Kalman filter.....	17



LIST OF FIGURES

Fig.2.1.1	Relation Motion between Inertial frame and Body frame	5
Fig.2.2.1	Location and Sensing direction of the nine accelerometers	12
Fig.2.4.1	Eular’ angle	21
Fig.2.5.1	The flow chart of all algorithms	22
Fig.3.2.1	Structure of uni-axis test	24
Fig.3.3.1	1HZ sin wave of function generator	24
Fig.3.3.2	11HZ sin wave of function generator	25
Fig.3.3.3	18HZ sin wave of function generator	25
Fig.3.4.1	Compare encoder and accelerometer output	26
Fig.3.5.1	angular rate representation in Body frame	28
Fig.3.5.2	angular rate representation in the Inertial frame	28
Fig.3.5.3	angular rate of Euler angles	29
Fig.3.5.4	Euler angles	29
Fig.3.5.5	Iterative convergence of angular rate representation in body frame	30
Fig.3.5.6	Linear acceleration representation in Body frame	30
Fig.3.5.7	Linear acceleration representation in Inertial frame	31

Fig.3.5.8	Angular rate in the rotation frame (R=50mm, std=0.1mm/s²)	31
Fig.4.1.1	Experimental procedure	35
Fig. 4.1.2	Algorithm flow	35
Fig.4.1.3	Circuit of low-pass analog amplifier (single pole)	36
Fig.4.1.4	Low-pass analog amplifier (single pole)	37
Fig.4.1.5	Butterworth low-pass filter (fourth order)	38
Fig.4.2.1	Experimental set up	40
Fig.4.2.2	Nine accelerometers output	41
Fig.4.2.3	Signals after Butterworth low-pass filter	41
Fig.4.2.4	Angular rate in the rotation frame	42
Fig.4.2.5	Angular rate in the rotation frame (simulation)	43
Fig.4.2.6	Angular displacement in the rotation frame	43
Fig.4.2.7	Euler's angular rate	44
Fig.4.2.8	Euler's angular rate ($(\omega_\phi + \omega_\varphi)$ in the third sub-figure)	44
Fig.4.2.9	Euler's angular displacement ($(\phi + \varphi)$ in the third sub-figure)	45
Fig.4.2.10	Angular rate in the inertial frame	45
Fig.4.2.11	Angular displacement in the inertial frame	46

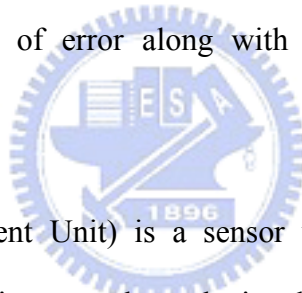
Fig.4.2.12	Linear acceleration in the rotation frame	47
Fig.4.2.13	Linear acceleration in the inertial frame	48
Fig.4.2.14	Linear acceleration in the inertial frame (with encoder information)	48
Fig4.3.1	Experimental set up	49
Fig4.3.2	Angular rate in the rotation frame	50
Fig4.3.3	Euler’s angular rate	50
Fig4.3.4	Angular rate in the inertial frame	52
Fig4.3.5	Angular rate in the inertial frame (with encoder information)	52
Fig4.3.6	Angular rate in the inertial frame (with encoder information)	53
Fig4.3.8	Linear acceleration in the rotation frame	54
Fig4.3.9	Linear acceleration in the inertial frame	54
Fig4.3.10	Linear acceleration in the inertial frame (with encoder information)	55
Fig4.4.1	Experimental set up	56
Fig.4.4.2	Angular rate in the rotation frame	57
Fig.4.4.3	Euler’s angular rate	58
Fig.4.4.4	Euler’s angular rate (with encoder information)	58

Fig.4.4.5	Angular rate in the inertial frame	59
Fig.4.4.6	Angular rate in the inertial frame (with encoder information)	59
Fig.4.4.7	Linear acceleration in the rotation frame	60
Fig.4.4.8	Linear acceleration in the inertial frame (with encoder information)	60
Fig.4.5.1	Vibration of tri-axes in the frequency domain	61
Fig.4.5.2	Vibration of tri-axes	62
Fig.4.5.3	Angular rate in the rotation frame (with linear vibration)	63
Fig.4.5.4	Linear accelerations in the rotation frame (with linear vibration)	63
Fig.4.5.5	Angular rate in the rotation frame (with rotational vibration)	64
Fig.4.5.6	Linear accelerations in the rotation frame (with rotational vibration)	65
Fig.4.5.7	Angular rate in the rotation frame (with 5Hz 100mm/s² DC-drift)	66
Fig.4.5.9	Angular rate in the rotation frame (with 1~17Hz 100mm/s² other noise)	67
Fig.4.5.10	Linear accelerations in the rotation frame (with 5Hz 100mm/s² other noise)	67

CHAPTER 1

INTRODUCTION

How to obtain the 6-DOF (3 linear motion and 3 angular motion) of a moving object with accuracy is one of the most important things in navigation. More and more sensors, which stem from different principles and measuring methods, have been utilized for the 6-DOF measurements. They include compass, INS (Inertial Navigation System), GPS (Global Positioning System) and etc. Combining INS and GPS is one of the most popular methods in-use today. That is because the satellite signal of the GPS is interrupted easily in certain region, and its update rate is not short enough for real-time application. On the other hand, the accumulation of error along with integral operation in INS can be erroneous [11].



IMU (Inertial Measurement Unit) is a sensor unit that can provide the position information (angular acceleration, angular velocity, linear acceleration and etc.) for an object in motion. Typical IMU uses three gyroscopes to sense the angular velocity and three linear accelerometers to sense the linear acceleration. The output from 3 gyroscopes undergoes one integral operation to obtain 3 rotation angles; and the output from 3 linear accelerometers undergoes two consecutive integration operations to obtain 3 coordinates for location. This approach has an acceptable angular rate sensing resolution but it is often expensive since 3 gyroscopes are incorporated. Because of which, the “Gyro-free IMU” was proposed 20 years ago. In the Gyro-free IMU, only linear accelerometers are utilized.

Recent development of Gyro-free IMU showed that workable schemes need, at least,

six accelerometers for a stable operation. Also, the output of these Gyro-free IMUs are 3 angular accelerations and 3 linear accelerations, which need 2 consecutive integral operations to obtain the rotation angle and 2 consecutive integral operations to obtain the 3 location coordinates in space. As compared to the IMU that is composed of 3 gyroscopes and 3 linear accelerometers, the gyro-free IMU needs one more integral operation and which would further deteriorate the sensing accuracy.

Due to the convergence properties of Gyro-free IMU, the accelerometers utilized must be deployed in a 3D location manner. As a consequence, the accelerometers must be fabricated in prior to the IMU and then mounted on the various locations of IMU. This approach inevitably results in misalignment error for the placement of accelerometers.

In correspondence to the existing problems mentioned above, we proposed the brand new design “observer-based planar Gyro-Free IMU” to solve these problems. In this design case, we incorporate nine accelerometers in the measurement unit, the output from six accelerometers are formulated for the governor equation of the measurement unit and the output of the other 1~3 accelerometers are for the system output, which will be utilized in the accompanied observer design. The key advantage of this observer-based gyro-free IMU operation is that the output of the IMU unit is angular rate, instead of angular acceleration, for the rotational motion measurement. As a consequence, we only need one integral operation to obtain the rotation angle, and thus the sensing accuracy is greatly increased.

In the conventional IMU approach, the accelerometers and/or gyroscopes have to be mounted onto the IMU cube in a 3-D manner for a stable operation. This approach inevitable bring upon the issues of alignment error and sensing accuracy. The proposed

method allows the accelerometers incorporated in the IMU be located on the same plane, which enables the in-situ fabrication of the accelerometers in the IMU. This approach increases the sensing accuracy of the IMU by minimize the alignment error of the accelerometers/gyroscopes incorporated.

The size of the gyro-free IMU is another determining factor for its sensing accuracy. Taking the centrifugal force of an object in circular motion for example, the acceleration along the centrifugal direction is of $\bar{\omega} \times (\bar{\omega} \times \bar{r})$. Therefore, a larger size of IMU (r) implies a smaller angular velocity ($\bar{\omega}$) that can be detected.

In order to obtain the equations the can describe the motion of the moving object in space concisely, we chose the coordinate that is fixed on the moving object and rotated with the object, which is often named “body frame”. Therefore, we need a transformation that can transform the motion information represented in body frame into inertial frame, which is the coordinate fixed to the earth center. There are many transformation methods that can carry on this operation, including: direction cosine, Euler’s angle and Euler’s parameters. “Direction cosine” is the simplest one, but it needs nine variables and thus could further complicate our algorithm. “Euler angle” method uses three variables but it need to calculate the trigonometric functions. “Euler’s parameters” is the most popular method for navigation system because it uses only four parameters and no need to calculating trigonometric functions. Here we chose the “Euler’s angle” method because it possessed the vivid physical meanings along the calculations. [4][5][6][7]

This paper is organized as follows. Chapter 2 introduces the theory and the algorithm of the “observer-base planar Gyro-Free IMU”. Chapter 3 shows the simulation results and preliminary test of single-axis stage with one accelerometer. Chapter 4 shows

our experiment setup and experimental results. Chapter 5 is the conclusion and future work.



CHAPTER 2

THEORY AND ALGORITHM

2.1 Motion of Rigid Body in Space

Fig.2.1.1 shows motion of point P in the space between inertial frame and body frame. O_i is the origin point of inertial frame and it is centroid of the earth. O_b is the origin point of body frame and it is centroid of aircraft. Equ.1 had been derived and it is used to explain acceleration of point P between inertial frame and body frame.

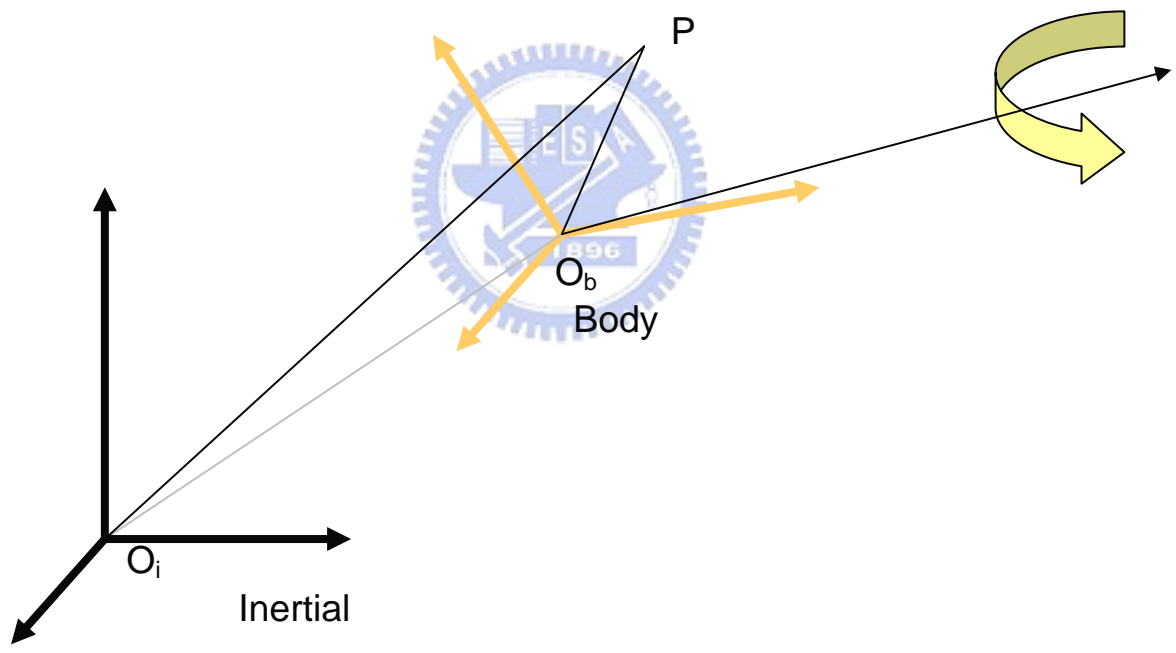


Fig. 2.1.1 Relation Motion between Inertial frame and Body frame

$$\vec{a} = \vec{\alpha} \times \vec{r} + \vec{a}_o + \vec{\omega} \times (\vec{\omega} \times \vec{r}) + 2\vec{\omega} \times \dot{\vec{r}} + \ddot{\vec{r}} \quad (2.1)$$

where

\vec{a} : Acceleration of point P,

\vec{a}_o : Acceleration of O_b ,

$\vec{\alpha}$: Angular acceleration of the body relative to inertial frame,

$\vec{\omega}$: Angular rate of the body relative to inertial frame,

\vec{r} : Location of point P relative to body frame,

$\dot{\vec{r}}$: Velocity of point P relative to body frame,

$\ddot{\vec{r}}$: Acceleration of point P related to body frame.

If the point P is fixed in the body frame and it is an accelerometer on the IMU, $\ddot{\vec{r}}, \dot{\vec{r}}$, $2\vec{\omega} \times \dot{\vec{r}}$ must be zero and acceleration of the point is given by:

$$\vec{a}^b = \vec{\alpha}^b \times \vec{r}^b + \vec{a}_o^b + \vec{\omega}^b \times (\vec{\omega}^b \times \vec{r}^b) \quad (2.2)$$

where,

\vec{a}^b : Acceleration of point P, representation in body frame,

\vec{a}_o^b : Acceleration of O_b , representation in body frame,

$\vec{\alpha}^b$: Angular acceleration of the body relative to inertial frame, representation in body frame,

$\vec{\omega}^b$: Angular rate of the body relative to inertial frame, representation in body frame,

2.2 Location of accelerometers and Dynamic system

Putting an accelerometer at the point P and $\bar{\eta}$ is the sensing direction of this accelerometer. Output of the accelerometer can be written as the form (2.3).

$$\begin{aligned}
 A &= \bar{\eta}^b \cdot \bar{a}^b \\
 &= \bar{\eta}^b \cdot (\bar{\alpha}^b \times \bar{r}^b) + \bar{\eta}^b \cdot \bar{a}_0^b + \bar{\eta}^b \cdot (\bar{\omega}^b \times (\bar{\omega}^b \times \bar{r}^b)) \\
 &= \bar{\alpha}^b \cdot (\bar{r}^b \times \bar{\eta}^b) + \bar{\eta}^b \cdot \bar{a}_0^b + \bar{\eta}^b \cdot (\bar{\omega}^b \times (\bar{\omega}^b \times \bar{r}^b))
 \end{aligned} \tag{2.3}$$

Because of there are six degrees of freedom, six accelerometers must be required at least. Six outputs of accelerometers can be constructed by matrix form. Formula (2.5) presents those on the body. Conveniently in use, J substitutes the relation between $\bar{\eta}$ and \bar{r} as shown in forming (2.4).

$$J \equiv \begin{bmatrix} (\bar{r}_1^b \times \bar{\eta}_1^b)^T & (\bar{\eta}_1^b)^T \\ (\bar{r}_2^b \times \bar{\eta}_2^b)^T & (\bar{\eta}_2^b)^T \\ (\bar{r}_3^b \times \bar{\eta}_3^b)^T & (\bar{\eta}_3^b)^T \\ (\bar{r}_4^b \times \bar{\eta}_4^b)^T & (\bar{\eta}_4^b)^T \\ (\bar{r}_5^b \times \bar{\eta}_5^b)^T & (\bar{\eta}_5^b)^T \\ (\bar{r}_6^b \times \bar{\eta}_6^b)^T & (\bar{\eta}_6^b)^T \end{bmatrix} \tag{2.4}$$

$$\begin{bmatrix} A_1 \\ A_2 \\ A_3 \\ A_4 \\ A_5 \\ A_6 \end{bmatrix} = \mathbf{J} \cdot \begin{bmatrix} \bar{\alpha}^b \\ \bar{a}_0^b \end{bmatrix} + \begin{bmatrix} (\bar{\eta}_1^b)^T \cdot (\bar{\omega}^b \times (\bar{\omega}^b \times \bar{r}_1^b)) \\ (\bar{\eta}_2^b)^T \cdot (\bar{\omega}^b \times (\bar{\omega}^b \times \bar{r}_2^b)) \\ (\bar{\eta}_3^b)^T \cdot (\bar{\omega}^b \times (\bar{\omega}^b \times \bar{r}_3^b)) \\ (\bar{\eta}_4^b)^T \cdot (\bar{\omega}^b \times (\bar{\omega}^b \times \bar{r}_4^b)) \\ (\bar{\eta}_5^b)^T \cdot (\bar{\omega}^b \times (\bar{\omega}^b \times \bar{r}_5^b)) \\ (\bar{\eta}_6^b)^T \cdot (\bar{\omega}^b \times (\bar{\omega}^b \times \bar{r}_6^b)) \end{bmatrix} \quad (2.5)$$

Formula (2.6) shows the relations between output signals of each accelerometer and dynamic properties of the body in motion and includes linear acceleration of aircraft, angular rate and angular acceleration that they are all represented in the rotation frame. There is an important issue with matrix J in Eq.2.6. In order to estimate angular acceleration and linear acceleration from (2.6), matrix J must be invertible. In other words, rank of J must be full rank. Formula (2.7) shows the “governing equation” in our model (IMU). Formula (2.8) presents the system output for observer to use. Formula (2.7) is an unstable system and there is white noise in practical application, so state estimation (observer) must be used to observe the real state without this noise. This question is taken up in the next section.

$$\begin{bmatrix} \bar{\alpha}^b \\ \bar{a}_0^b \end{bmatrix} = \mathbf{J}^{-1} \cdot \left(\begin{bmatrix} A_1 \\ A_2 \\ A_3 \\ A_4 \\ A_5 \\ A_6 \end{bmatrix} - \begin{bmatrix} (\bar{\eta}_1^b)^T \cdot (\bar{\omega}^b \times (\bar{\omega}^b \times \bar{r}_1^b)) \\ (\bar{\eta}_2^b)^T \cdot (\bar{\omega}^b \times (\bar{\omega}^b \times \bar{r}_2^b)) \\ (\bar{\eta}_3^b)^T \cdot (\bar{\omega}^b \times (\bar{\omega}^b \times \bar{r}_3^b)) \\ (\bar{\eta}_4^b)^T \cdot (\bar{\omega}^b \times (\bar{\omega}^b \times \bar{r}_4^b)) \\ (\bar{\eta}_5^b)^T \cdot (\bar{\omega}^b \times (\bar{\omega}^b \times \bar{r}_5^b)) \\ (\bar{\eta}_6^b)^T \cdot (\bar{\omega}^b \times (\bar{\omega}^b \times \bar{r}_6^b)) \end{bmatrix} \right) \quad (2.6)$$

$$[\bar{\alpha}^b] = J^{-1}(1:3,:) \cdot \left(\begin{array}{c} \mathbf{A}_1 \\ \mathbf{A}_2 \\ \mathbf{A}_3 \\ \mathbf{A}_4 \\ \mathbf{A}_5 \\ \mathbf{A}_6 \end{array} \cdot \left[\begin{array}{c} (\bar{\eta}_1^b)^T \cdot (\bar{\omega}^b \times (\bar{\omega}^b \times \bar{r}_1^b)) \\ (\bar{\eta}_2^b)^T \cdot (\bar{\omega}^b \times (\bar{\omega}^b \times \bar{r}_2^b)) \\ (\bar{\eta}_3^b)^T \cdot (\bar{\omega}^b \times (\bar{\omega}^b \times \bar{r}_3^b)) \\ (\bar{\eta}_4^b)^T \cdot (\bar{\omega}^b \times (\bar{\omega}^b \times \bar{r}_4^b)) \\ (\bar{\eta}_5^b)^T \cdot (\bar{\omega}^b \times (\bar{\omega}^b \times \bar{r}_5^b)) \\ (\bar{\eta}_6^b)^T \cdot (\bar{\omega}^b \times (\bar{\omega}^b \times \bar{r}_6^b)) \end{array} \right] \right) \quad (2.7)$$

$$\begin{bmatrix} \mathbf{A}_7 \\ \mathbf{A}_8 \\ \mathbf{A}_9 \end{bmatrix} = \begin{bmatrix} (\bar{r}_7^b \times \bar{\eta}_7^b)^T \\ (\bar{r}_8^b \times \bar{\eta}_8^b)^T \\ (\bar{r}_9^b \times \bar{\eta}_9^b)^T \end{bmatrix} \cdot \begin{bmatrix} (\bar{\eta}_7^b)^T \\ (\bar{\eta}_8^b)^T \\ (\bar{\eta}_9^b)^T \end{bmatrix} \cdot J^{-1} \cdot \left(\begin{array}{c} \mathbf{A}_1 \\ \mathbf{A}_2 \\ \mathbf{A}_3 \\ \mathbf{A}_4 \\ \mathbf{A}_5 \\ \mathbf{A}_6 \end{array} \cdot \left[\begin{array}{c} (\bar{\eta}_1^b)^T \cdot (\bar{\omega}^b \times (\bar{\omega}^b \times \bar{r}_1^b)) \\ (\bar{\eta}_2^b)^T \cdot (\bar{\omega}^b \times (\bar{\omega}^b \times \bar{r}_2^b)) \\ (\bar{\eta}_3^b)^T \cdot (\bar{\omega}^b \times (\bar{\omega}^b \times \bar{r}_3^b)) \\ (\bar{\eta}_4^b)^T \cdot (\bar{\omega}^b \times (\bar{\omega}^b \times \bar{r}_4^b)) \\ (\bar{\eta}_5^b)^T \cdot (\bar{\omega}^b \times (\bar{\omega}^b \times \bar{r}_5^b)) \\ (\bar{\eta}_6^b)^T \cdot (\bar{\omega}^b \times (\bar{\omega}^b \times \bar{r}_6^b)) \end{array} \right] \right) + \begin{bmatrix} (\bar{\eta}_7^b)^T \cdot (\bar{\omega}^b \times (\bar{\omega}^b \times \bar{r}_7^b)) \\ (\bar{\eta}_8^b)^T \cdot (\bar{\omega}^b \times (\bar{\omega}^b \times \bar{r}_8^b)) \\ (\bar{\eta}_9^b)^T \cdot (\bar{\omega}^b \times (\bar{\omega}^b \times \bar{r}_9^b)) \end{bmatrix} \quad (2.8)$$

In order to ensure matrix J invertible, designing the relation between location and sensing direction becomes an important issue. One way we used is that putting nine accelerometers in the same circular on the flat, Fig. 2 illustrates the location and sensing direction about all accelerometers and Table 1 shows these parameters. Location and sensing direction of the first three and 7th, 8th accelerometers sense the tangential acceleration, the 4th to 6th accelerometers sense acceleration of Z-axis only and 9th accelerometer sense the centripetal acceleration. Matrix J can be rewritten as (2.9) and the determinant of matrix J is not zero as shown in formula (2.10).

$$J = \begin{bmatrix} 0 & 0 & 1 & \eta_{11} & \eta_{12} & 0 \\ 0 & 0 & 1 & \eta_{21} & \eta_{22} & 0 \\ 0 & 0 & 1 & \eta_{31} & \eta_{32} & 0 \\ r_{42} & -r_{41} & 0 & 0 & 0 & 1 \\ r_{52} & -r_{51} & 0 & 0 & 0 & 1 \\ r_{62} & -r_{61} & 0 & 0 & 0 & 1 \end{bmatrix} \quad (2.9)$$

Where, η_{nm}, r_{nm} n : nth accelerometer,

M : mth coordinate base.

$$\det(J) = -\eta_{21}\eta_{32}r_{52}r_{61} + \eta_{12}\eta_{21}r_{41}r_{52} \neq 0 \quad (2.10)$$

Table 1 Location and Sensing direction of the accelerometers

	Location $\vec{r}_j^T = [x, y, z]$	Sensing direction $\vec{\eta}_j^T = [x, y, z]$
Accelerometer 1	$\left[\cos\left(\frac{4\pi}{9}\right), \sin\left(\frac{4\pi}{9}\right), 0 \right]$	$\left[\cos\left(\frac{17\pi}{9}\right), \sin\left(\frac{17\pi}{9}\right), 0 \right]$
Accelerometer 2	$\left[\cos\left(\frac{10\pi}{9}\right), \sin\left(\frac{10\pi}{9}\right), 0 \right]$	$\left[\cos\left(\frac{-7\pi}{9}\right), \sin\left(\frac{-7\pi}{9}\right), 0 \right]$
Accelerometer 3	$\left[\cos\left(\frac{16\pi}{9}\right), \sin\left(\frac{16\pi}{9}\right), 0 \right]$	$\left[\cos\left(\frac{5\pi}{9}\right), \sin\left(\frac{5\pi}{9}\right), 0 \right]$

Accelerometer 4	$\left[\cos\left(\frac{2\pi}{9}\right), \sin\left(\frac{2\pi}{9}\right), 0 \right]$	$[0,0,1]$
Accelerometer 5	$\left[\cos\left(\frac{8\pi}{9}\right), \sin\left(\frac{8\pi}{9}\right), 0 \right]$	$[0,0,1]$
Accelerometer 6	$\left[\cos\left(\frac{14\pi}{9}\right), \sin\left(\frac{14\pi}{9}\right), 0 \right]$	$[0,0,1]$
Accelerometer 7	$\left[\cos\left(\frac{6\pi}{9}\right), \sin\left(\frac{6\pi}{9}\right), 0 \right]$	$\left[\cos\left(\frac{7\pi}{6}\right), \sin\left(\frac{7\pi}{6}\right), 0 \right]$
Accelerometer 8	$\left[\cos\left(\frac{12\pi}{9}\right), \sin\left(\frac{12\pi}{9}\right), 0 \right]$	$\left[\cos\left(\frac{-\pi}{6}\right), \sin\left(\frac{-\pi}{6}\right), 0 \right]$
Accelerometer 9	$[1,0,0]$	$[1,0,0]$

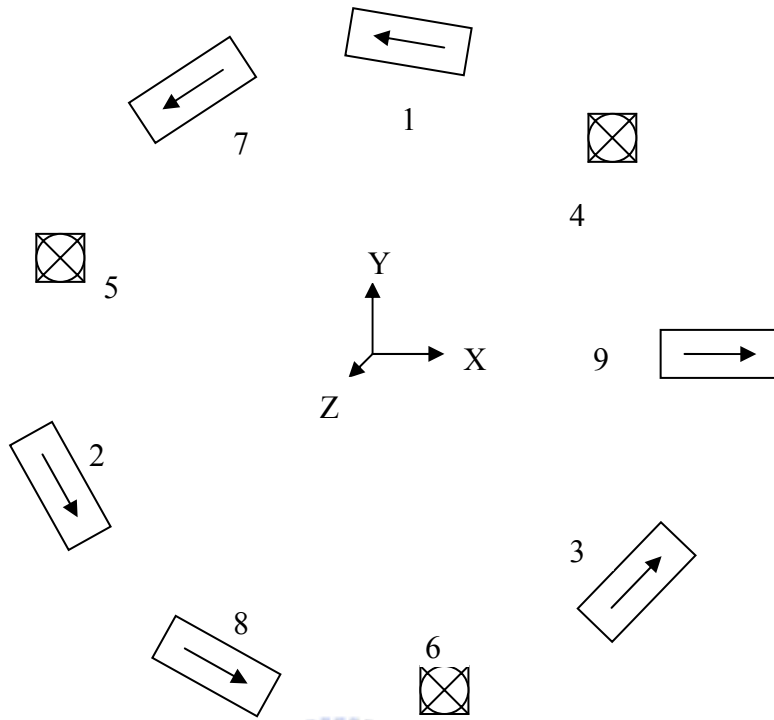


Fig.2.2.1 Location and Sensing direction of the nine accelerometers

According to the above parameters of accelerometers, governing equation (2.7) and output equation (2.8) can be rewritten as (2.11) (2.12).

$$\begin{bmatrix} \dot{\omega}_1^b \\ \dot{\omega}_2^b \\ \dot{\omega}_3^b \end{bmatrix} = J^{-1}(1:3,:) \cdot \begin{bmatrix} A_1 \\ A_2 \\ A_3 \\ A_4 \\ A_5 \\ A_6 \end{bmatrix} + \begin{bmatrix} -\omega_2^b \omega_3^b \\ \omega_1^b \omega_3^b \\ a_1(\omega_1^b)^2 + a_2(\omega_2^b)^2 + (a_1 + a_2)(\omega_3^b)^2 + a_3 \omega_1^b \omega_2^b \end{bmatrix} \quad (2.11)$$

$$\begin{bmatrix} A_7 \\ A_7 \\ A_7 \end{bmatrix} = ACoef1 \cdot \begin{bmatrix} A_1 \\ A_2 \\ A_3 \\ A_4 \\ A_5 \\ A_6 \end{bmatrix} + ACoef2 \cdot \begin{bmatrix} (\omega_1^b)^2 + (\omega_3^b)^2 \\ (\omega_2^b)^2 + (\omega_3^b)^2 \\ \omega_1^b \omega_3^b \end{bmatrix} \quad (2.12)$$

Formula (2.11) and (2.12) present the dynamic system in the continuous time domain.

In order to program the above system, $\dot{\omega}_j$ can be discretize by $\omega_j(k+1)$, $\omega_j(k)$ and dt as formula (2.13). Formula (2.14) and (2.15) show the discrete system from (2.11) and (2.12) by (2.13).

$$\dot{\omega}_j = \frac{\omega_j(k+1) - \omega_j(k)}{dt} \quad (2.13)$$

$$\begin{bmatrix} \omega_1^b(k+1) \\ \omega_2^b(k+1) \\ \omega_3^b(k+1) \end{bmatrix} = J^{-1}(1:3,:) \cdot \begin{bmatrix} A_1(k) \\ A_2(k) \\ A_3(k) \\ A_4(k) \\ A_5(k) \\ A_6(k) \end{bmatrix} \cdot dt + \begin{bmatrix} -\omega_2^b(k)\omega_3^b(k) \\ \omega_1^b(k)\omega_3^b(k) \\ a_1(\omega_1^b(k))^2 + a_2(\omega_2^b(k))^2 + (a_1 + a_2)(\omega_3^b(k))^2 + a_3\omega_1^b(k)\omega_2^b(k) \end{bmatrix} \cdot dt + \begin{bmatrix} \omega_1^b(k) \\ \omega_2^b(k) \\ \omega_3^b(k) \end{bmatrix} \quad (2.14)$$

$$\begin{bmatrix} A_7(k) \\ A_8(k) \\ A_9(k) \end{bmatrix} = ACoeff1 \cdot \begin{bmatrix} A_1(k) \\ A_2(k) \\ A_3(k) \\ A_4(k) \\ A_5(k) \\ A_6(k) \end{bmatrix} + ACoeff2 \cdot \begin{bmatrix} (\omega_1^b(k))^2 + (\omega_3^b(k))^2 \\ (\omega_2^b(k))^2 + (\omega_3^b(k))^2 \\ \omega_1^b(k)\omega_3^b(k) \end{bmatrix} \quad (2.15)$$

2.3 Kalman filter

2.3.1 The Extended Kalman Filter

Consider the nonlinear system with dynamics

$$x(k+1) = f[k \quad x(k)] + v(k) \quad (2.16)$$

where, for simplicity, it is assumed that there is no control, and the noise is assumed additive, zero mean, and white Gaussian distribution.

$$E[v(k)] = 0 \quad E[v(k)v(j)'] = R(k)\delta_{kj} \quad (2.17)$$

The measurement is

$$z(k) = h[k \quad x(k)] + \omega(k) \quad (2.18)$$

Where the measurement noise is additive, zero mean, and white

$$E[\omega(k)] = 0 \quad E[\omega(k)\omega(j)'] = R(k)\delta_{kj} \quad (2.19)$$

Because of this is a nonlinear system, the system need to be linearization. Formula (2.20) uses Taylor series expansion to linearize system and measurement for obtaining the optima estimation of the system.

$$\begin{aligned} x(k+1) &= f\left[k, \hat{x}(k|k) + f_x(k)[x(k) - \hat{x}(k|k)] + \frac{1}{2} \sum_{i=1}^{n_x} e_i [x(k) - \hat{x}(k|k)]' f_{xx}^i(k)[x(k) - \hat{x}(k|k)]\right] \\ &\quad + \text{HOT} + v(k) \end{aligned} \quad (2.20)$$

where

e_i : i^{th} Cartesian basis vector,

$f_x(k) \equiv \frac{\partial f}{\partial x} \equiv \left[\nabla_x f(k, x) \right]' \Big|_{x=\hat{x}(k|k)}$: the Jacobian of vector f ,

$f_{xx}^i(k) \equiv \frac{\partial^2 f^i}{\partial x^2} \equiv \left[\nabla_x \nabla_x' f^i(k, x) \right]' \Big|_{x=\hat{x}(k|k)}$: the Hessian of vector f ,

HOT : higher-order terms.

State prediction

The predicted state to time $k+1$ from time k is obtained by taking the expectation of (2.20) neglecting HOT.

$$\hat{x}(k+1|k) = f[k, \hat{x}(k|k)] + \frac{1}{2} \sum_{i=1}^{n_x} e_i \text{tr} [f_{xx}^i P(k|k)] \quad (2.21)$$

And prediction covariance is:

$$P(k+1|k) = f_x(k) P(k|k) f_x'(k) + \frac{1}{2} \sum_{i=1}^{n_x} \sum_{j=1}^{n_x} e_i e_j' \text{tr} [f_{xx}^i(k) P(k|k) f_{xx}^j(k) P(k|k)] + Q(k) \quad (2.22)$$

Measurement prediction

Similarly, the predicted measurement is, for the second-order filter

$$\hat{z}(k+1|k) = h[k+1, \hat{x}(k+1|k)] + \frac{1}{2} \sum_{i=1}^{n_z} e_i \text{tr} [h_{xx}^i(k+1) P(k+1|k)] \quad (2.23)$$

The measurement prediction covariance or innovation covariance or residual covariance--really MSE matrix—is

$$\begin{aligned}
 S(k+1) &= h_x(k+1)P(k+1|k)h_x(k+1)' \\
 &+ \frac{1}{2} \sum_{i=1}^{n_x} \sum_{j=1}^{n_x} e_i e_j' \text{tr} [h_{xx}^i(k+1)P(k+1|k)h_{xx}^j(k+1)P(k+1|k)] + R(k+1)
 \end{aligned} \tag{2.24}$$

Filter gain

$$W(k+1) = P(k+1)h_x(k+1)'S(k+1)^{-1} \tag{2.25}$$

Update

The state estimate updated is

$$\hat{x}(k+1|k+1) = \hat{x}(k+1|k) + W(k+1)v(k+1) \tag{2.26}$$

and state covariance updated is

$$P(k+1|k+1) = P(k+1|k) - W(k+1)S(k+1)W(k+1)' \tag{2.27}$$

The optima estimation will obtain from the above calculating repeatedly.

Using the first-order extended Kalman filter, the higher-order term and the Hessian of f , and h will be neglected. For simplify to use the first order extended Kalman filter, Table 2 is presented the flow chat included state prediction and state update.

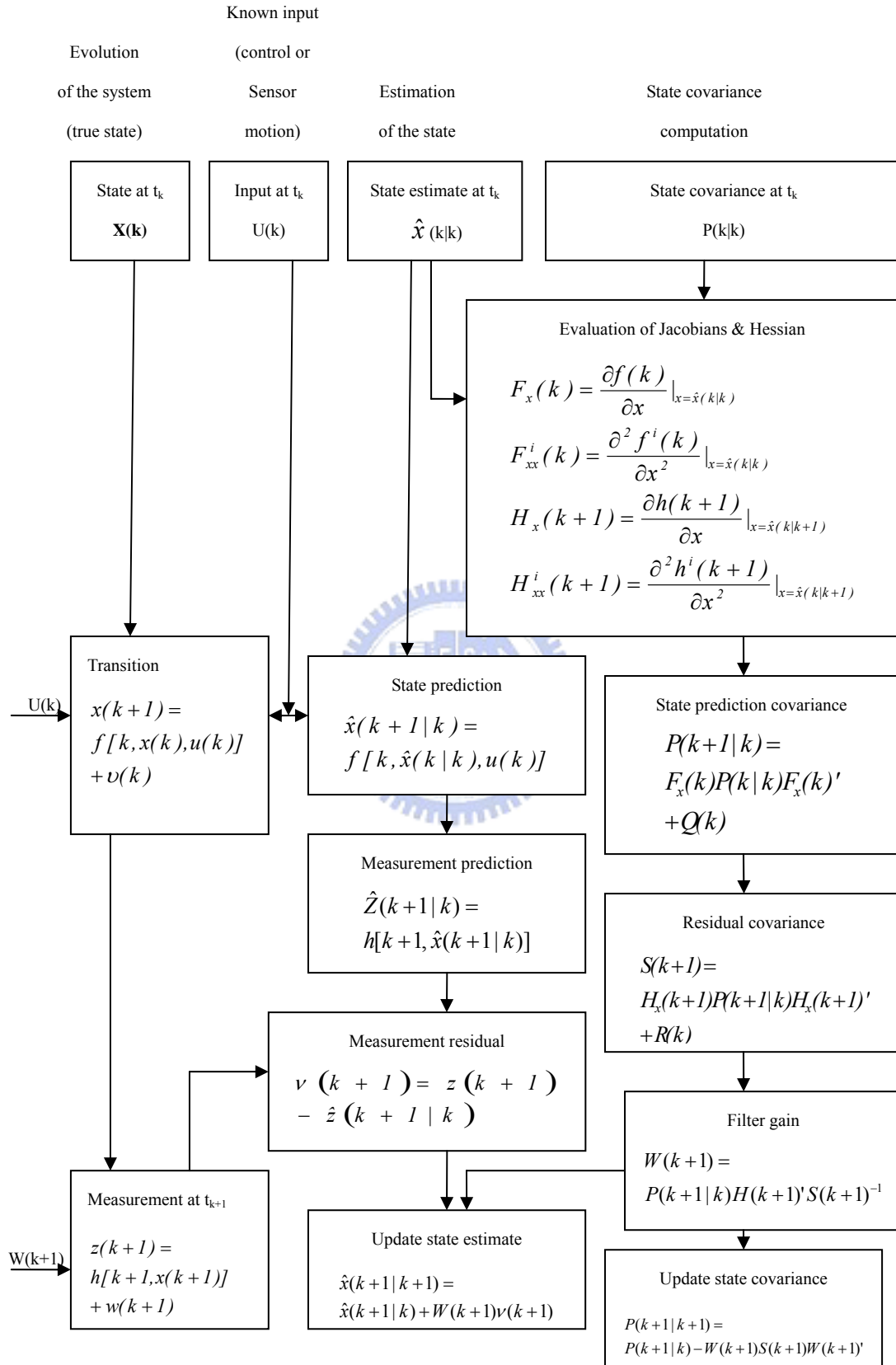


Table 2 Flow chart of first order Extended Kalman filter

2.3.2 The Iterated Extended Kalman Filter

A modified state updating approach can be obtained by an iterative procedure as follows.

$$H^i \equiv h_x [k+1, \hat{x}^i(k+1|k+1)] \quad (2.28)$$

$$\begin{aligned} P^i(k+1|k+1) &= P(k+1|k) \\ &- P(k+1|k)H^i(k+1)' \left[H^i(k+1)P(k+1|k)H^i(k+1)' + R(k+1) \right]^{-1} H^i(k+1)P(k+1|k)' \end{aligned} \quad (2.29)$$

$$\begin{aligned} \hat{x}^{i+1}(k+1|k+1) &= \hat{x}^i(k+1|k+1) \\ &+ P^i(k+1|k+1)H^i(k+1)' R(k+1)^{-1} \{z(k+1) - h[k+1, \hat{x}^i(k+1|k+1)]\} \\ &- P^i(k+1|k+1)P(k+1|k)^{-1} [\hat{x}^i(k+1|k+1) - \hat{x}(k+1|k)] \end{aligned} \quad (2.30)$$

Starting the iteration for $i = 0$ with

$$\hat{x}^0(k+1|k+1) \equiv \hat{x}(k+1|k)$$

causes the last term in (2.30) to be zero and yields after the first iteration $\hat{x}^1(k+1|k+1)$, that is, the same as the first-order (no iterated) EKF.

Overview of the Iteration Sequence

For $i=(0:N-1)$

(2.28)

(2.29)

(2.30)

For $i=N$

(2.30)

with N decided either a priori or based on a convergence criterion.

Through the above procedure to calculate angular rate and linear acceleration represented in body frame repeatedly, we can obtain the optima estimation at time $k + 1$.

2.4 Orthogonal Transfer Matrix

In order to consider the angular rate and linear represented in inertial frame, the orthogonal matrix should be used to transfer the representation to another base which interests us. Formula (2.31) shows the relation between two different bases.

$$X^b = AX^i \tag{2.31}$$

Where

X^b : Representation in body frame,

A : Orthogonal transfer matrix,

X^i : Representation in inertial frame.

The Euler angles θ , ϕ and φ are an orthogonal transform to transfer the quantities in the rotation frame into those in the inertial frame.

Fig.2.4.1 shows the sequence that is started by rotating the initial system of axes, XYZ, by an angle ϕ counterclockwise about the Z axis, and the resultant coordinate system is labeled the $\xi\eta\zeta$ axes. In the second step, the intermediate axes, $\xi\eta\zeta$, are rotated about the η axis counterclockwise by the angle θ to produce another intermediate set, the $\xi'\eta'\zeta'$ axes. Finally, the $\xi'\eta'\zeta'$ axes are rotated counterclockwise by an angle φ about the ζ' axis to produce the desired X'Y'Z' system of axes. Follow the above three separate rotation is called Y-Convention. Formulas (2.32) to (2.34) show the relation like (2.31) in the three rotations. Formula (2.35) shows the result of the three separate rotations, and A is the orthogonal transfer matrix defined in formula (2.31). Formula (2.36) shows inverse A to transfer representation from the body frame to the inertial frame.

$$\xi = DX^i \quad (2.32)$$

$$\xi' = C\xi \quad (2.33)$$

$$X^b = B\xi' \quad (2.34)$$

$$A = BCD$$

$$= \begin{bmatrix} \cos \phi & \sin \phi & 0 \\ -\sin \phi & \cos \phi & 0 \\ 0 & 0 & 1 \end{bmatrix} \begin{bmatrix} \cos \theta & 0 & -\sin \theta \\ 0 & 1 & 0 \\ \sin \theta & 0 & \cos \theta \end{bmatrix} \begin{bmatrix} \cos \phi & \sin \phi & 0 \\ -\sin \phi & \cos \phi & 0 \\ 0 & 0 & 1 \end{bmatrix}$$

(2.35)

$$X^i = A^{-1}X^b = A'X^b$$

$$A' = D'C'B'$$

$$= \begin{bmatrix} \cos \phi & -\sin \phi & 0 \\ \sin \phi & \cos \phi & 0 \\ 0 & 0 & 1 \end{bmatrix} \begin{bmatrix} \cos \theta & 0 & \sin \theta \\ 0 & 1 & 0 \\ -\sin \theta & 0 & \cos \theta \end{bmatrix} \begin{bmatrix} \cos \phi & -\sin \phi & 0 \\ \sin \phi & \cos \phi & 0 \\ 0 & 0 & 1 \end{bmatrix}$$

(2.36)

$$= \begin{bmatrix} -\sin \phi \sin \phi + \cos \theta \cos \phi \cos \phi & -\sin \phi \cos \phi - \cos \theta \sin \phi \cos \phi & \cos \sin \theta \\ \cos \phi \sin \phi + \cos \theta \cos \phi \sin \phi & \cos \phi \cos \phi - \cos \theta \sin \phi \sin \phi & \sin \sin \theta \\ \sin \theta \cos \phi & \sin \theta \sin \phi & \cos \theta \end{bmatrix}$$

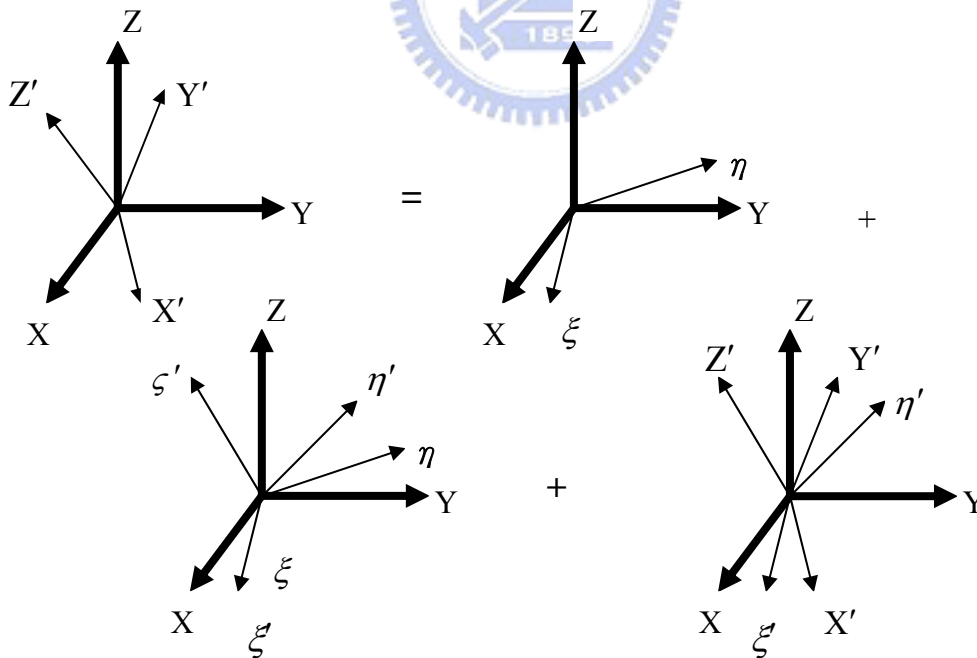


Fig.2.4.1 Euler' angle

It is often convenient to express the angular rate vector in terms of Euler angles and

their time derivatives as (2.37). In consequence of the vector property of infinitesimal rotations, the vector Euler angles time derivatives can be obtained as the sum of the three separate angular rate vectors and ω . The angle θ must avoid being zero carefully, or make the element in the (2.37) singular.

$$\begin{bmatrix} \dot{\phi} \\ \dot{\theta} \\ \dot{\phi} \end{bmatrix} = \begin{bmatrix} \frac{-\cos \varphi}{\sin \theta} & \frac{\sin \varphi}{\sin \theta} & 0 \\ \sin \varphi & \cos \varphi & 0 \\ \frac{\cos \theta \cos \varphi}{\sin \theta} & \frac{-\cos \theta \sin \varphi}{\sin \theta} & 1 \end{bmatrix} \begin{bmatrix} \omega_x \\ \omega_y \\ \omega_z \end{bmatrix} \quad (2.37)$$

2.5 Flow chart

Fig.2.5.1 shows the procedure how to use these accelerometers to obtain all information in the body frame or inertial frame.

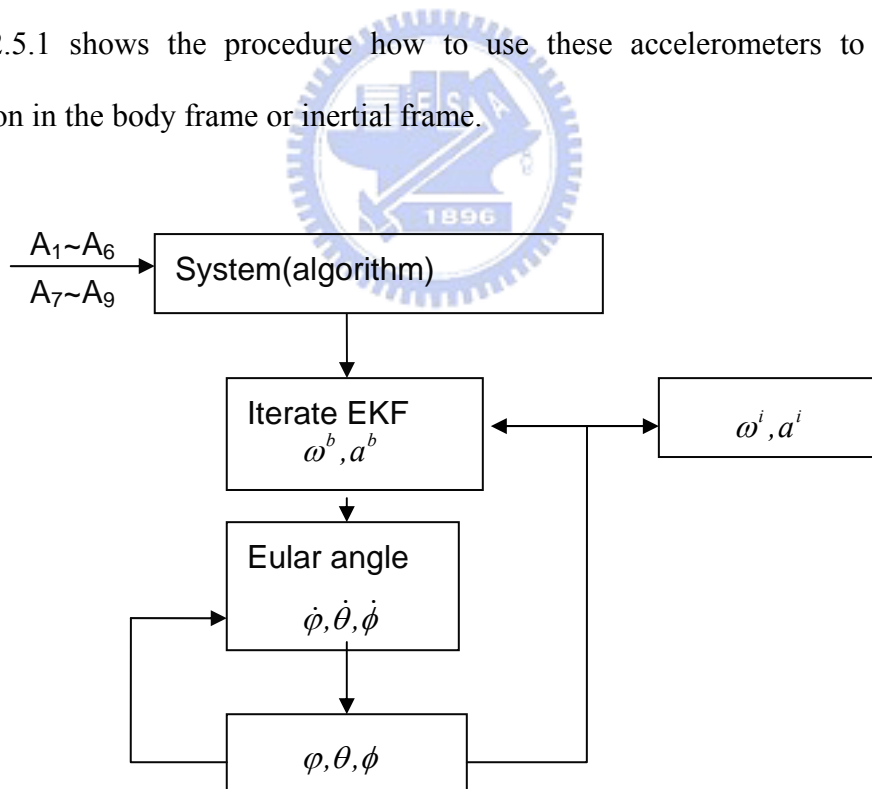


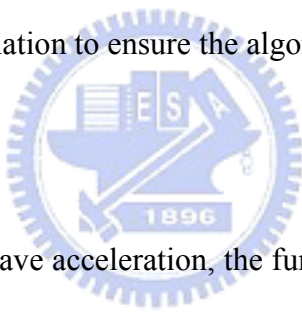
Fig.2.5.1 The flow chart of all algorithms

CHAPTER 3

SIMULATION AND PRELIMINARY TEST

The algorithm introduced in Chapter 2 will be proved by simulating with Matlab package. In this proof, consider about the random noise with accelerometer output will be measured from static-tested of an accelerometer on a stage. In order to make sure that the experiments are accurate, we test the response of one axis with one accelerometer at first. The structure of test will be presented in section 3.2. Section 3.3 shows that how to simulate the motion and define the suitable accelerometer output signal. Section 3.4 shows that preliminary tested from an accelerometer in the above motion we defined. Section 3.5 shows Matlab simulation to ensure the algorithm we derived in Chapter 2.

3.1 Test structure



In order to get pure sine wave acceleration, the function generator employs to provide PWM servo amplifiers command and those drives the DC motor on the stage. The stage is driven by Dc motor and generates a sinusoidal acceleration which is less than 1g. And the output of accelerometer (ADXL105) is set to a nominal scale factor of 250 mV/g. However, in order to reduce SNR and increase accuracy, the circuits used to amplify output voltage must be needed.

Information of encoder of the DC motor is measured by motion card (ADLINK PCI-8133) and the accelerometer output signals are measured by DAQ card (ADLINK PCI-9114). Then, we need 2 consecutive integral operations to obtained displacement of stage and compare those with encoder information. Fig.3.2.1 shows the block diagram of the test system.

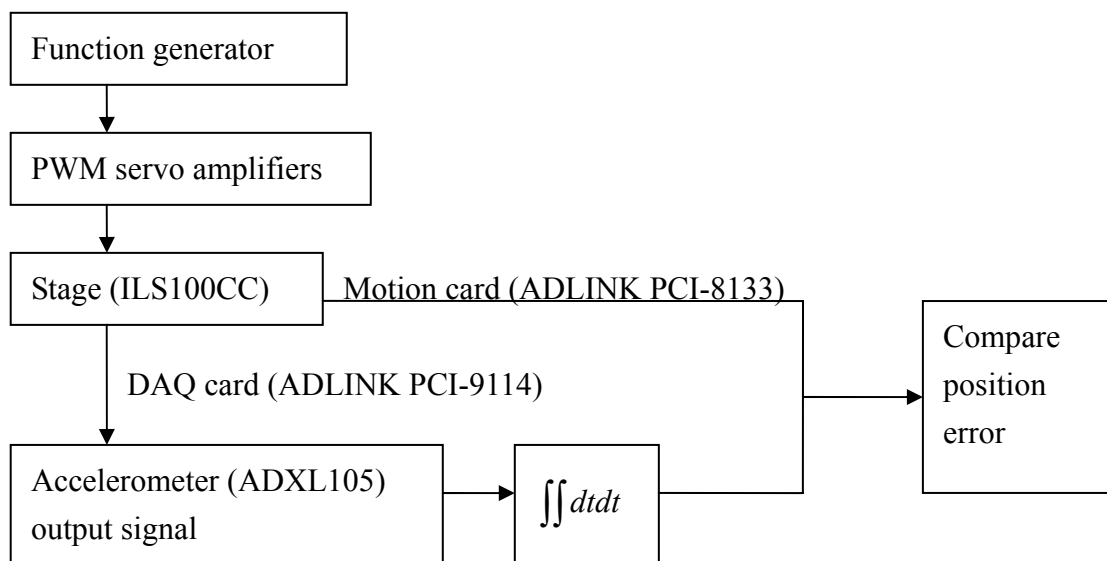


Fig.3.2.1 Structure of uni-axis test

3.2 Generate Motion

Pure sine wave assists us to analysis the signal easily. It is different between the input commands of the DC motor from the output of accelerometer, because it loses the energy on stage. In order to make sure that the signal is the pure sin wave, tuning the frequency of the function generator until the differential data of encoder twice to be like the pure sinusoidal response. Fig.3.3.1 to Fig.3.3.3 shows the result of these procedures.

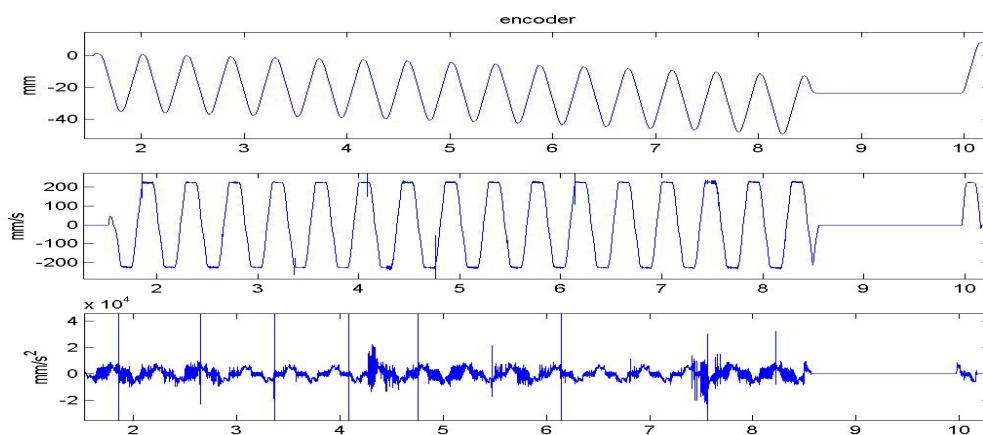


Fig.3.3.1 1HZ sin wave of function generator

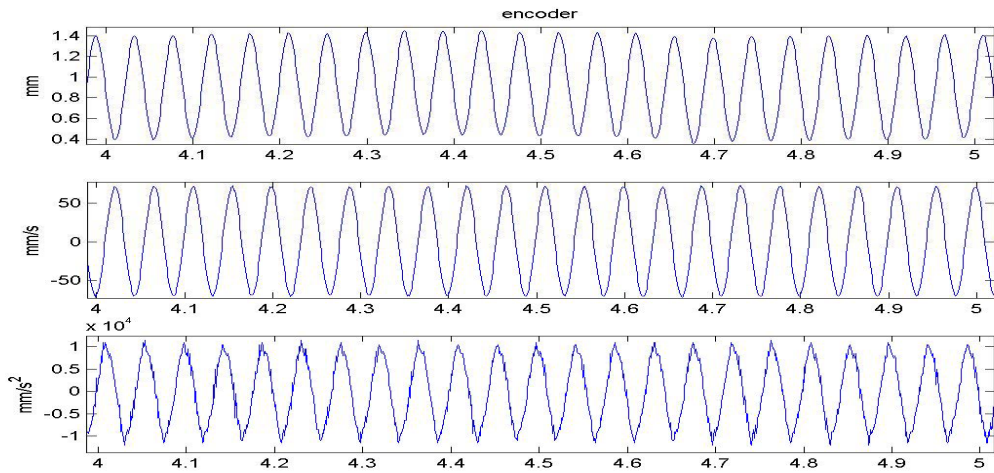


Fig.3.3.2 11HZ sin wave of function generator

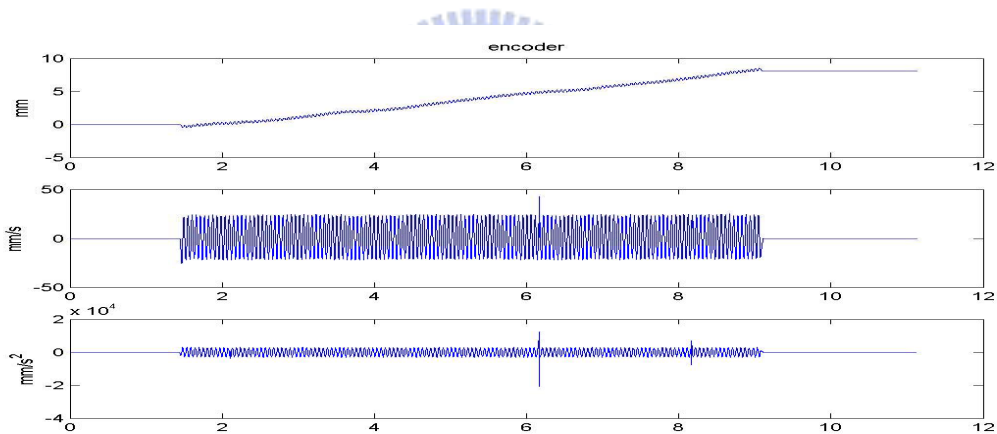


Fig.3.3.3 18HZ sin wave of function generator

We can obtain the result that we increase the frequency of the function generator and the acceleration becomes pure sine wave. If we increase the frequency of the function generator over than about 20HZ, we will get the smaller amplitude of the acceleration than before. Finally, 18HZ of the function generator is employed to be the input command in this one axis tested.

3.3 One Axis Tested

In the above condition, the acceleration output will be measured by DAQ card. Fig.3.4.1 shows the acceleration output, the data which is obtained by integrating the output of accelerometer once or twice, and we compare those with the information of the encoder. The accumulation of integral error can be indicated clearly as shown in Fig.3.4.1. The source of this error is the drift of the accelerometer output and the vibration of optical table. This question is taken up in the chapter.5.

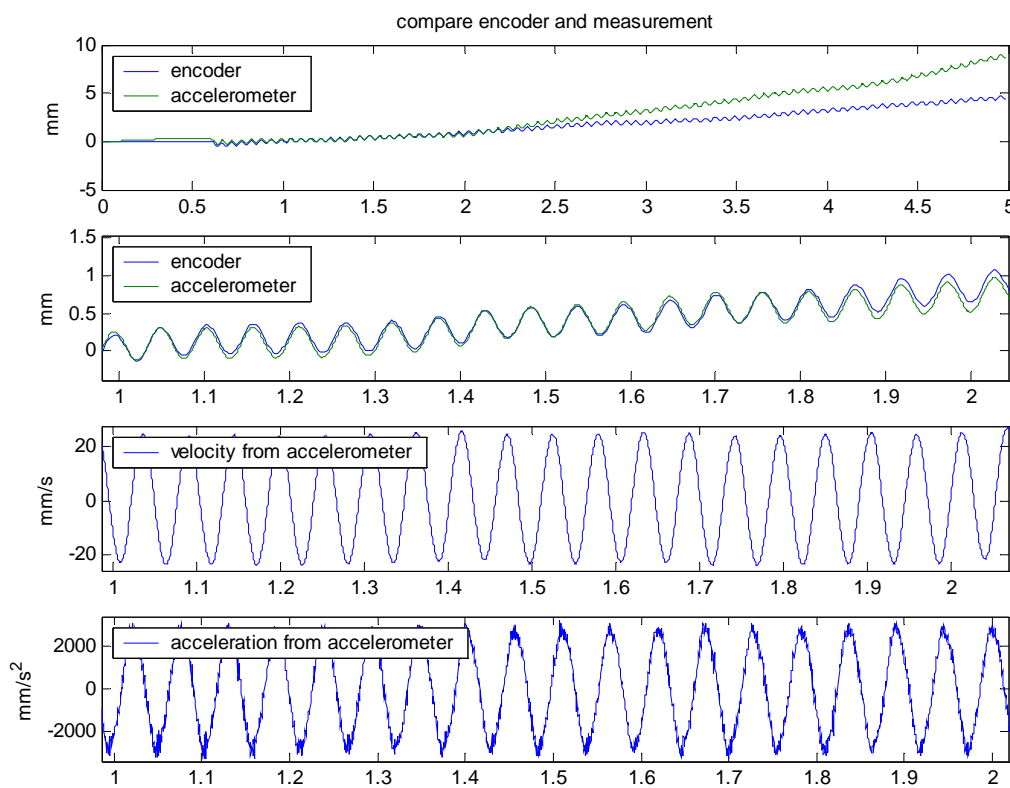


Fig.3.4.1 Compare encoder and accelerometer output

The sampling rate of encoder is 500 HZ and the sampling rate of DAQ card is 2000 HZ. When the DC motor is static, the standard deviation is 21.9416 mm/s^2 . The amplify scale is $1000/39$, the operator voltage is 0V and 5V and the accelerometer output scale is 250 mV/g, so acceleration must be smaller than $0.39g$ (3900 mm/s^2) with

these conditions. Formula 3.1 shows the result.

$$(5V/2)*(39/1000)/(0.25)=0.39 \quad (3.1)$$

3.4 Simulation and Resolution

We define the path of the angular acceleration of the Euler's angles and linear accelerations in the inertial frame as formula(3.2). We assume that sampling rate of DAQ card is 1000HZ, $l=50\text{mm}$ and the standard deviation is $25\text{mm}/s^2$.

$$\begin{bmatrix} \dot{\phi} \\ \dot{\theta} \\ \dot{\psi} \end{bmatrix} = \begin{bmatrix} 2 \times \pi/3 \\ 2 \times \pi/3 \\ 2 \times \pi/3 \end{bmatrix} \quad (\text{rad/s})$$

$$\begin{bmatrix} A_x \\ A_y \\ A_z \end{bmatrix} = \begin{bmatrix} 2000 \times \sin(2 \times \pi \times 18 \times t) \\ 2000 \times \sin(2 \times \pi \times 18 \times t) \\ 2000 \times \sin(2 \times \pi \times 18 \times t) \end{bmatrix} \quad (\text{mm/s}^2) \quad (3.2)$$

Fig.3.5.1 shows the state of the algorithm we derived and Fig.3.5.2 shows the angular rate in the inertial frame.

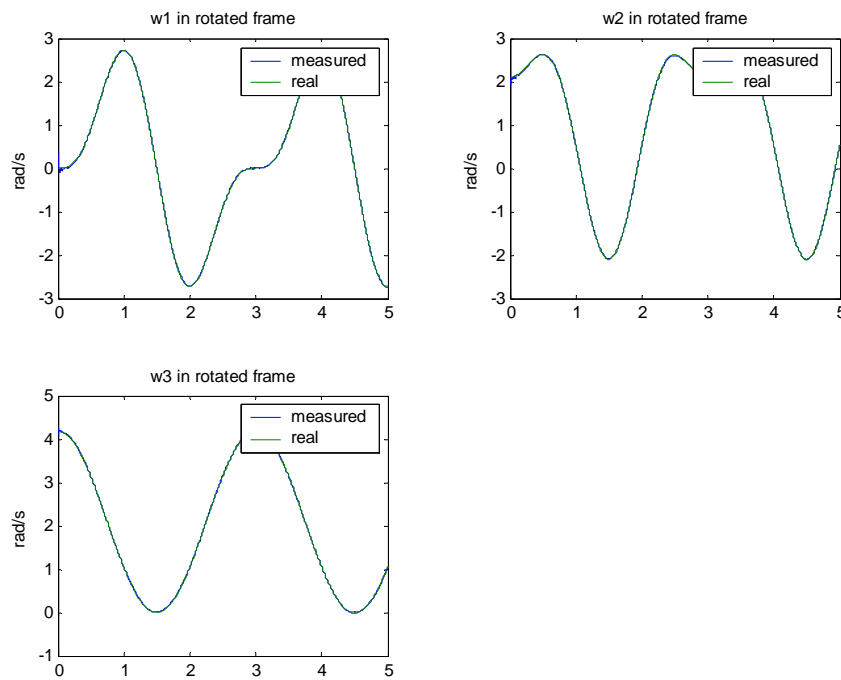


Fig.3.5.1 angular rate representation in Body frame

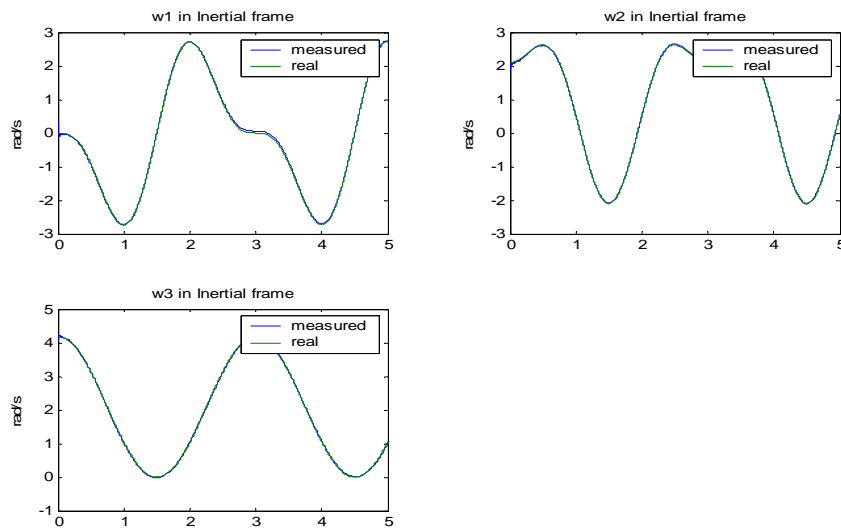


Fig.3.5.2 angular rate representation in the Inertial frame

Fig.3.5.3 shows the Euler's angular rate and Fig.3.5.4 shows the Euler's angle. There is pulse at 1.5, 3 and 4 seconds, because the matrix in formula (2.37) is singular.

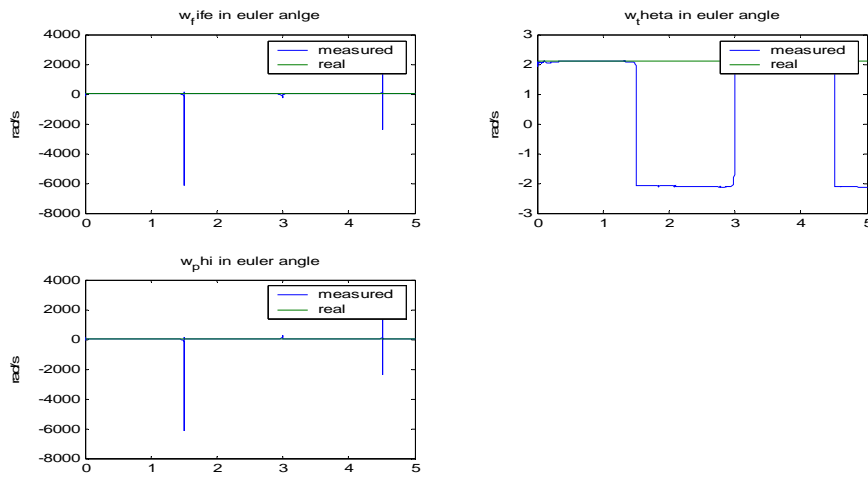


Fig.3.5.3 angular rate of Euler angles

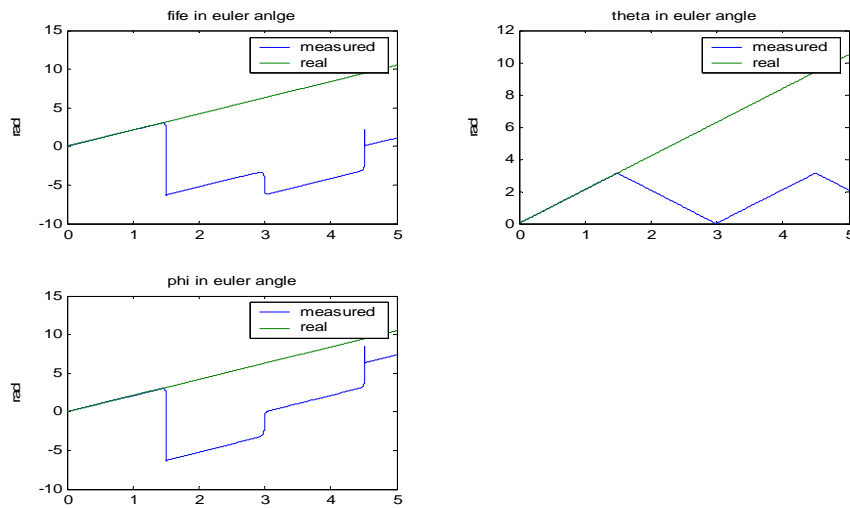


Fig.3.5.4 Euler angles

The iterative time is 40 for initial to 0.1 second and 20 for 0.1 second to 1 second.

Fig.3.5.5 shows the result of iteration.

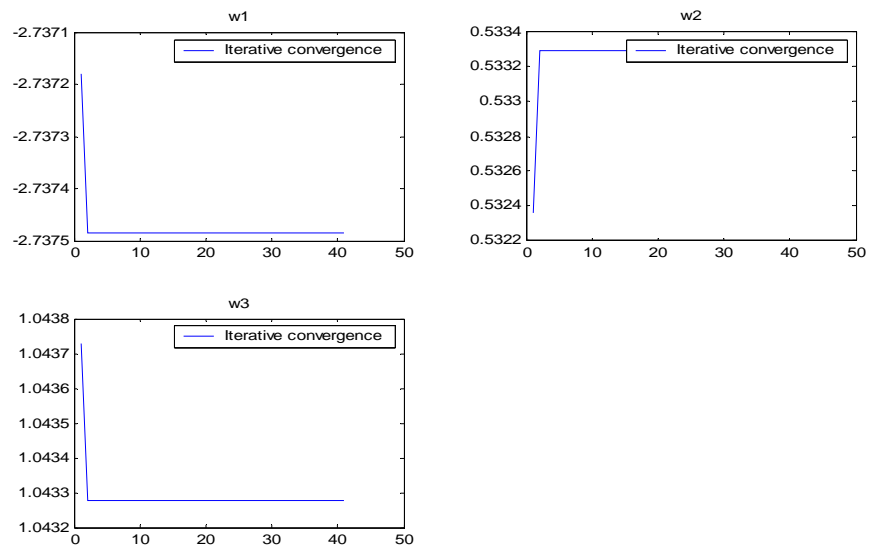


Fig.3.5.5 Iterative convergence of angular rate representation in body frame

Fig.3.5.6 shows the linear accelerations in the body frame and Fig.3.5.7 shows the linear accelerations in the inertial frame.

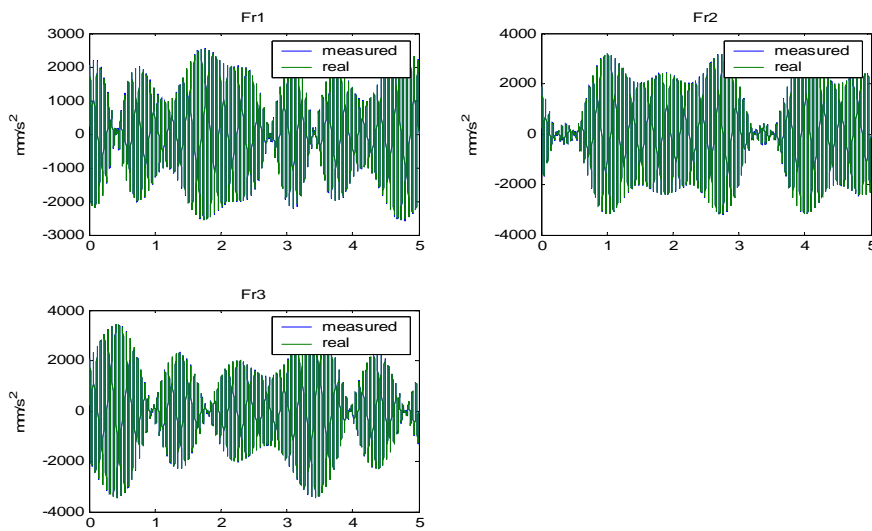


Fig.3.5.6 Linear acceleration representation in Body frame

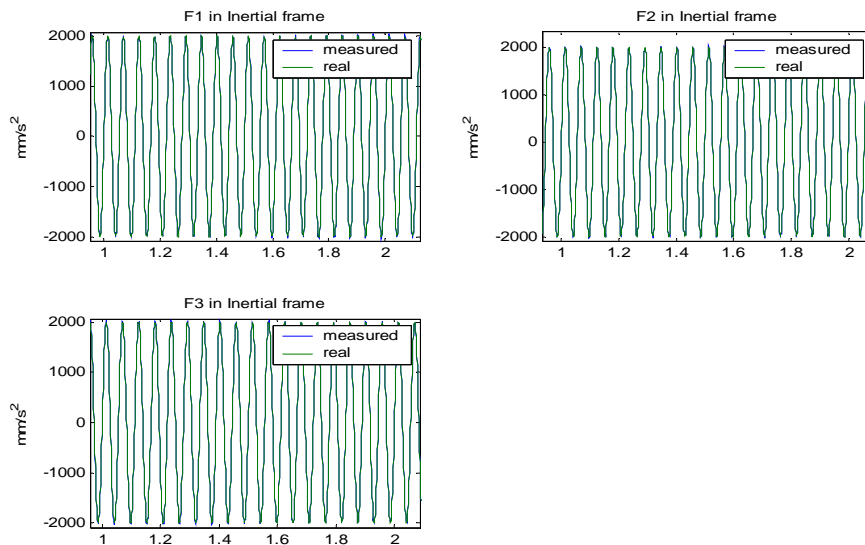


Fig.3.5.7 Linear acceleration representation in Inertial frame

Resolution

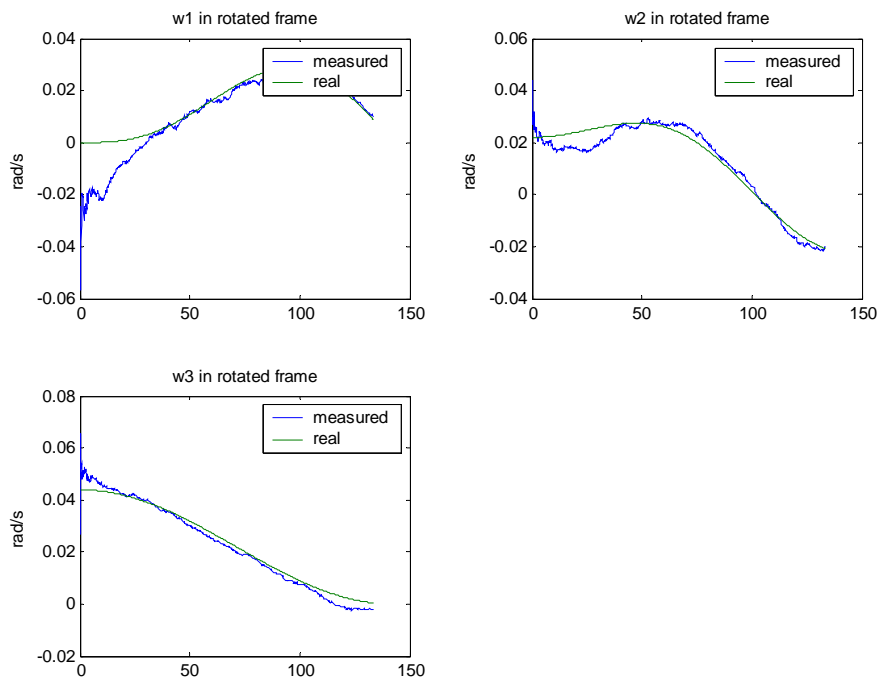


Fig.3.5.8 Angular rate in the rotation frame ($R=50\text{mm}$, $\text{std}=0.1\text{mm/s}^2$)

Fig.3.5.8 shows the angular rate in the rotation frame with $R=50\text{mm}$, standard deviation (std)= 0.1mm/s^2 and resolution is $12^\circ/\text{s}$. We assume that the angular

acceleration and linear acceleration is zero, and rewrite Eq.2.3 as Eq.3.3. We can find out the relationship between resolution of accelerometer and angular rate of our algorithm shown as Eq.3.4.

$$\begin{aligned}
 A &= \bar{\eta}^b \cdot \bar{a}^b \\
 &= \bar{\eta}^b \cdot (\bar{\alpha}^b \times \bar{r}^b) + \bar{\eta}^b \cdot \bar{a}_0^b + \bar{\eta}^b \cdot (\bar{\omega}^b \times (\bar{\omega}^b \times \bar{r}^b)) \\
 &= \bar{\eta}^b \cdot (\bar{\omega}^b \times (\bar{\omega}^b \times \bar{r}^b)) \\
 \Rightarrow A &\propto r\omega^2
 \end{aligned} \tag{3.3}$$

$$\Rightarrow \omega \propto \sqrt{\frac{A}{r}} \tag{3.4}$$



CHAPTER 4

TEST OF THE IMU DESIGN

To verify the feasibility and reliability of the method for computing angular rate, it is necessary to perform a two-step validation procedure, i.e., the method has to yield consistent and accurate results while acquiring data both from hypothetical and experimental systems.

To check if our method is feasible for any arbitrary motion, some experiments with different configurations should be done. According to the type of Euler's angle (ZYZ convention), we design three different experiments and simulations. First, Z axis in the body frame is parallel to the axis of rotation and the other two linear motions are parallel to the inertial frame. Secondly, initial condition is changed in order to verify the observer method is practical when acceleration of gravity effect on the output of accelerometer. Thirdly, Y axis in body frame is parallel to the axis of rotation and the other two linear motions are parallel to the inertial frame.

Section 4.1 describes the procedures for these experiments with the designed motion, analog amplifier, and Butterworth filter. Section 4.2, 4.3 and 4.4 describes the first, second and third experiment and simulation, respectively.

4.1 Experimental procedure

Basic procedure of experiment, analog low-pass amplifier, Butterworth filter and designed motion will be introduced in this section, and variation of tri-axial setup will be present in the following section.

Basic procedure of experiment

Three different function generators output sinusoidal voltage to three different PWM servo amplifiers. These servo amplifiers output sinusoidal current to three different stages. Sinusoidal current excite sinusoidal acceleration on the stage and we put our IMU on the stage to sense the sinusoidal acceleration and read the encoder information by motion card (ADLINK PCI-8133). System noise or disturbance will be generated when three stages create the sinusoidal. And the acceleration output of the ADXL105 is nominally 250mV/g. This scale factor is not appreciated for our applications. An amplifier is need to set an appreciate scale ratio and a low-pass filter is needed to filter accelerometer's internal or circuit high-frequency noise, so analog 1-pole low-pass filter will be employed to filter those between accelerometer and DAQ card (ADLINK PCI-9114). But other high-frequency noise will be excited when data of acceleration are transferred between the output of 1-pole low-pass filter and DAQ card. The digital filter (4th order Butterworth filter) must be needed to filter this noise by computer. Let the result of digital filter be as acceleration output ($A_1 \sim A_9$) shown as in algorithm, and physical quantities can be calculated by our observer base IMU. To compare these quantities and encoder's information, and we will know our algorithm be practical or not. We will discuss every physical quantities which interest us to be practical or not in the following sections. Fig.4.1.1 and Fig.4.1.2 show the process of experiment and the flow chart of algorithm respectively.

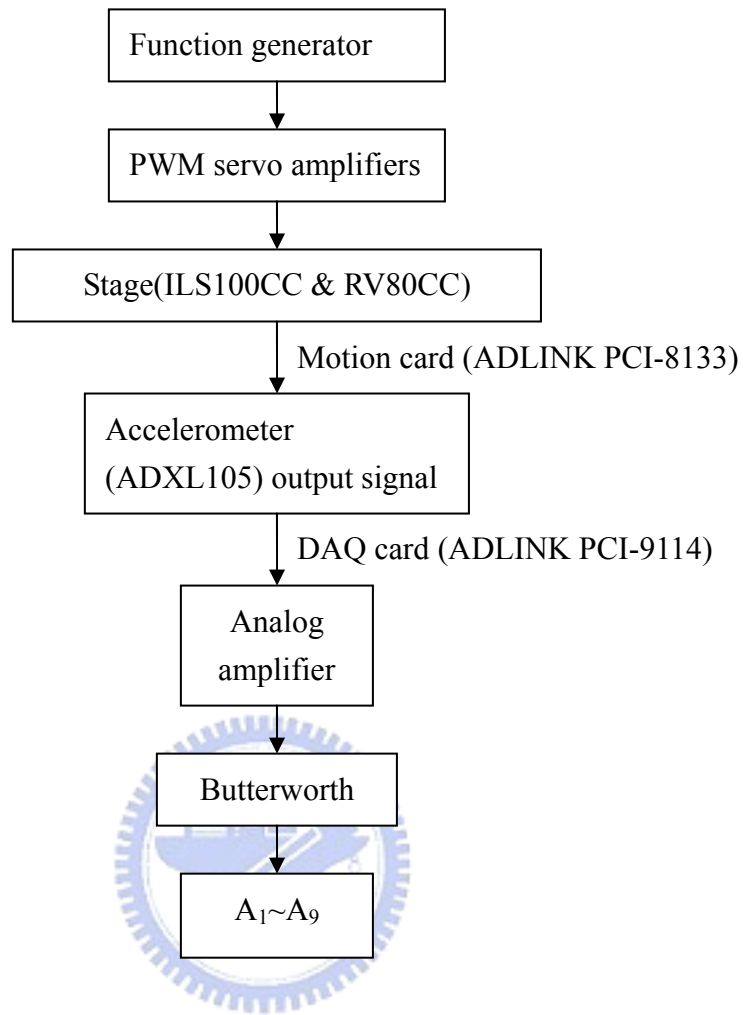


Fig.4.1.1 Experimental procedure

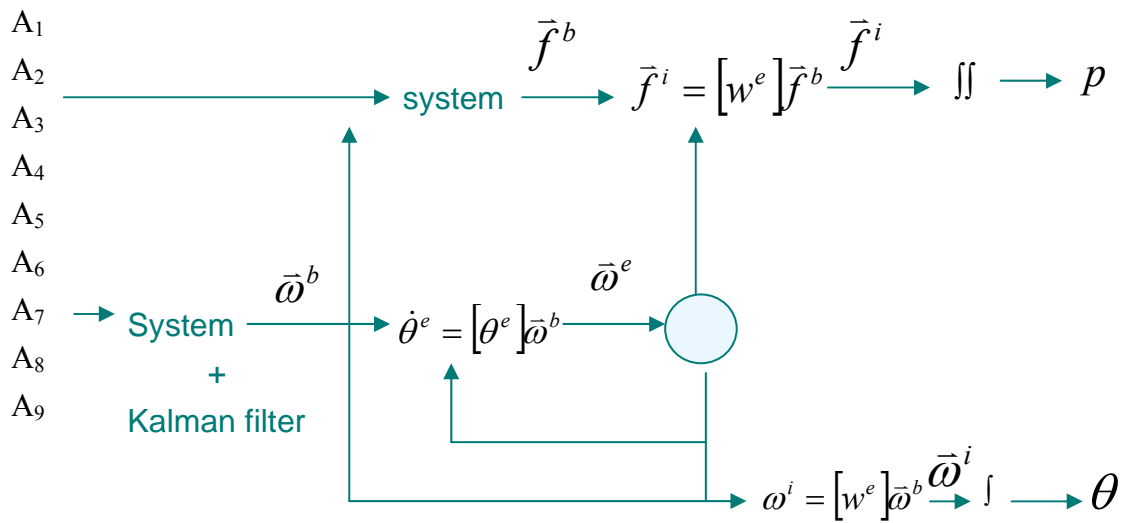


Fig. 4.1.2 Algorithm flow

Route of motion

Because sinusoidal current excited sinusoidal acceleration on the stage, Eq.4.1 describes the relationship about displacement, velocity and acceleration. Fig.3.4.1 shows tendency of Eq.4.1.

$$\text{Acceleration} = \sin(2\pi ft)$$

$$\text{Velocity} = -\frac{1}{2\pi f} \cos(2\pi ft) + \frac{1}{2\pi f}$$

$$\text{Displacement} = -\frac{1}{(2\pi f)^2} \sin(2\pi ft) + \frac{1}{2\pi f} t$$

(4.1)

Low-pass analog amplifier (single pole)

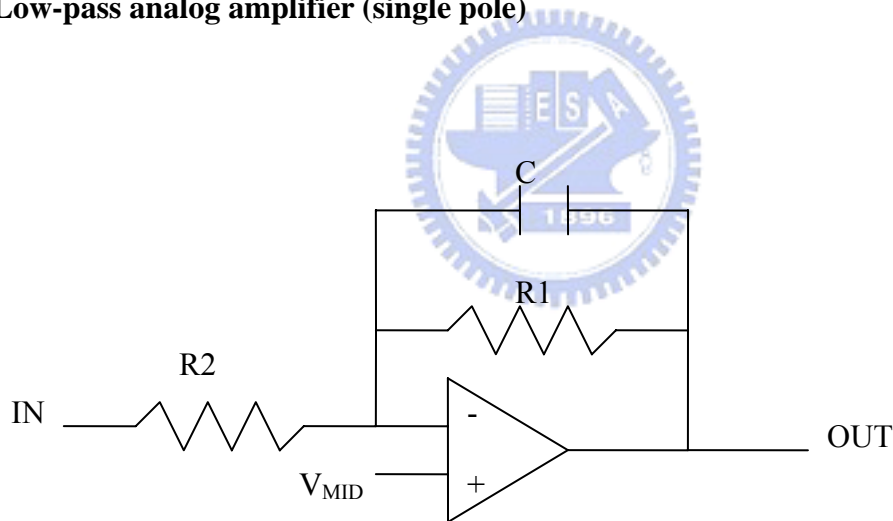


Fig.4.1.3 Circuit of low-pass analog amplifier (single pole)

Fig.4.1.3 presents the circuit of low-pass filter and Fig.4.1.4 shows the Bode plot of low-pass filter. Eq.4.2 describes the gain is 5.1282 and Eq.4.3 shows the transfer function when the cutoff frequency is 117.0257 HZ, and.

$$f_{-3dB} = \frac{1}{2\pi CR}$$

$$\text{GAIN} = -\frac{R1}{R2} \tag{4.2}$$

$$R1 = 200K\Omega \quad R2 = 39K\Omega$$

$$C = 6.8 \times 10^{-9} \text{F}$$

$$T = \frac{5.128}{0.00136s + 1} \tag{4.3}$$

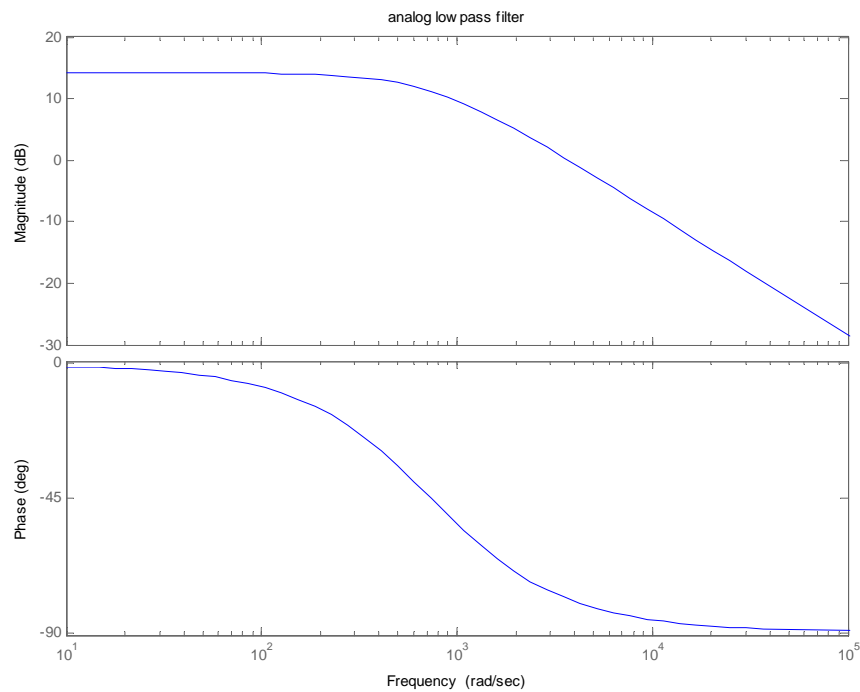


Fig.4.1.4 Low-pass analog amplifier (single pole)

Butterworth filter

Butterworth filters are characterized by a magnitude response that is maximally flat in the pass-band and monotonic overall. Butterworth filters sacrifice roll-off steepness for monotonic in the pass- and stop-bands. Unless the smoothness of the Butterworth filter is

needed, an elliptic or Chebyshev filter can generally provide steeper roll-off characteristics with a lower filter order. Eq.4.4 shows the Z-transform and Fig.4.1.5 shows frequency response when data sampled at 2000 Hz and design a 4th-order low-pass Butterworth filter with cutoff frequency of 50 Hz.

$$H(Z) = \frac{3.12 \times 10^{-5} + 1.25 \times 10^{-4} Z^{-1} + 1.87 \times 10^{-4} Z^{-2} + 1.25 \times 10^{-4} Z^{-3} + 3.12 \times 10^{-5} Z^{-4}}{1 - 3.5897 Z^{-1} + 4.38513 Z^{-2} - 2.9241 Z^{-3} - 6.6301 \times 10^{-1} Z^{-4}} \quad (4.4)$$

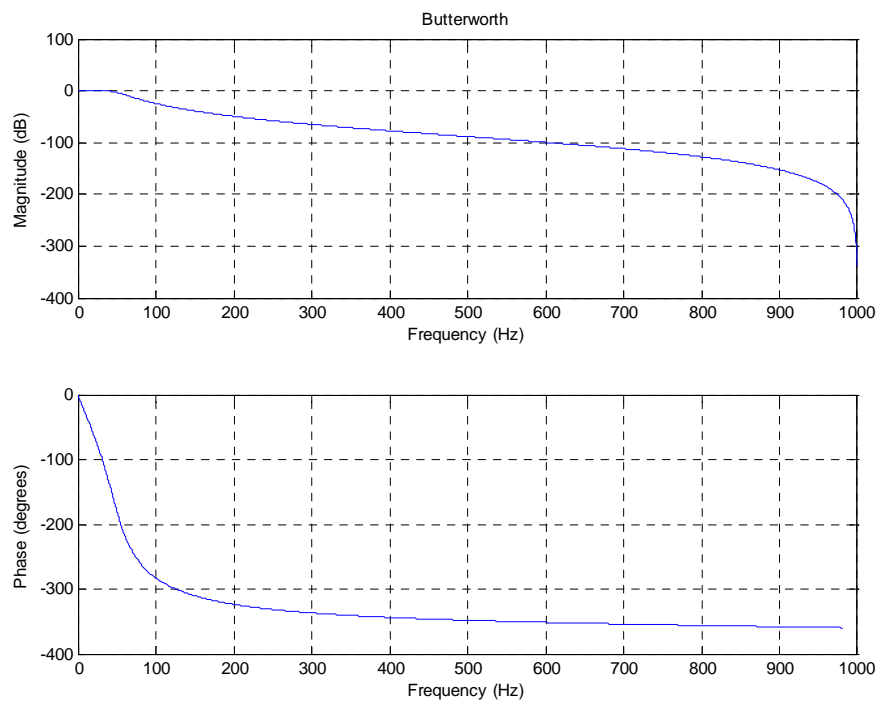


Fig.4.1.5 Butterworth low-pass filter (fourth order)

There is invariably a time delay between a demodulated signal and the original received signal. The Butterworth filter parameters directly affect the length of this delay.

4.2 Z-axis rotation with biaxial linear acceleration

In this experiment, Z axis in body frame is parallel to the axis of rotation and the other two linear motions are parallel to X axis and Y axis in the inertial frame respectively. Fig.4.2.1 shows this experiment setup. Eq.4.5 presents Euler' s transform in these condition. Generally speaking, whether the quantity of Z-axis in the rotation frame or in the inertial frame must be equal to the Euler' s angle $(\phi + \varphi)$, and the quantities of X-axis, Y-axis and Euler' s angle θ must be zero. But that is not exact correct in practical experiment. We shall now look more carefully into Eq.4.5, the quantity of Z-axis must be equal to the Euler' s angle $(\phi + \varphi)$ when the disturbance or noise in the Euler' s angle θ is close to zero, and the quantity of Z-axis is equal to φ when the disturbance or noise in the Euler' s angle θ is larger then a value which is over than 0.06 radian after 0.2 seconds in this experiment. Compared Fig.4.2.7 with Fig.4.2.8, and we can clearly understand this question. Fig.4.2.2 shows accelerations which are through analog low-pass filter and Fig.4.2.3 shows accelerations which are through analog low-pass filter and then are through digital Butterworth low-pass filter. The curve in Fig.4.2.3 is smoother then in Fig.4.2.2 and in Fig.4.2.3; there is invariably a time delay which is introduced in the above section. In Fig.4.2.4 and Fig.4.2.6~4.2.13, the information of encoder shown by solid line, result of estimated shown by dotted line and subtracting time delay shown by dash-dot line. The rule holds in the flowing two sections.

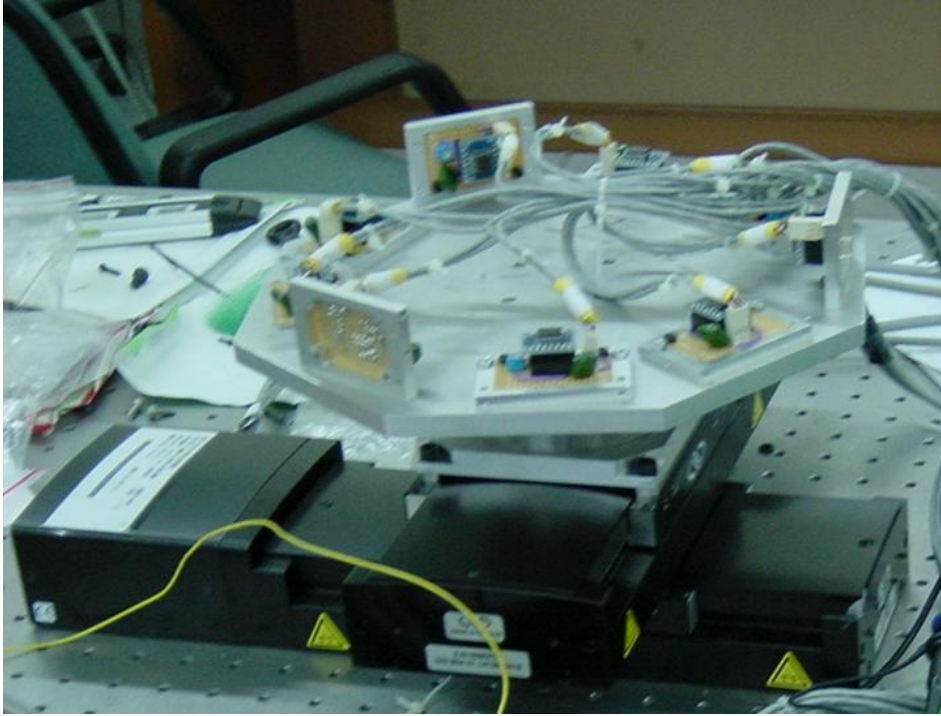


Fig.4.2.1 Experimental set up

$$\begin{aligned}
 \theta = 0 \\
 X^i &= \begin{bmatrix} \cos \phi & -\sin \phi & 0 \\ \sin \phi & \cos \phi & 0 \\ 0 & 0 & 1 \end{bmatrix} \begin{bmatrix} \cos \theta & 0 & \sin \theta \\ 0 & 1 & 0 \\ -\sin \theta & 0 & \cos \theta \end{bmatrix} \begin{bmatrix} \cos \phi & -\sin \phi & 0 \\ \sin \phi & \cos \phi & 0 \\ 0 & 0 & 1 \end{bmatrix} X^b \\
 &= \begin{bmatrix} -\sin \phi \sin \phi + \cos \phi \cos \phi & -\sin \phi \cos \phi - \sin \phi \cos \phi & 0 \\ \cos \phi \sin \phi + \cos \phi \sin \phi & \cos \phi \cos \phi - \sin \phi \sin \phi & 0 \\ 0 & 0 & 1 \end{bmatrix} X^b \\
 &= \begin{bmatrix} \cos(\phi + \phi) & -\sin(\phi + \phi) & 0 \\ \sin(\phi + \phi) & \cos(\phi + \phi) & 0 \\ 0 & 0 & 1 \end{bmatrix} X^b
 \end{aligned} \tag{4.5}$$

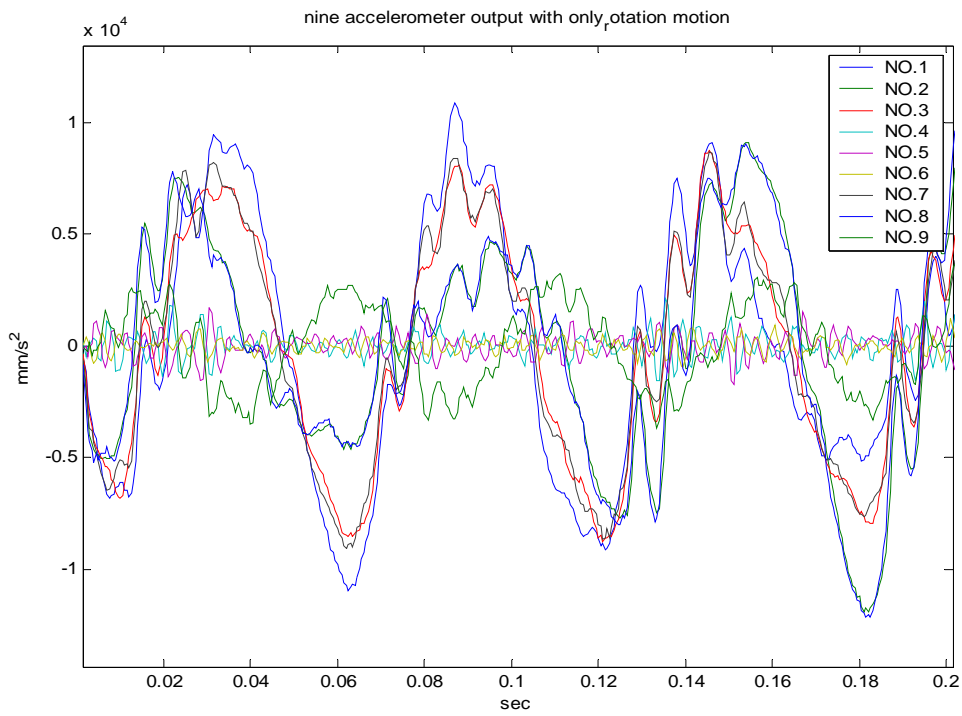


Fig.4.2.2 Nine accelerometers output

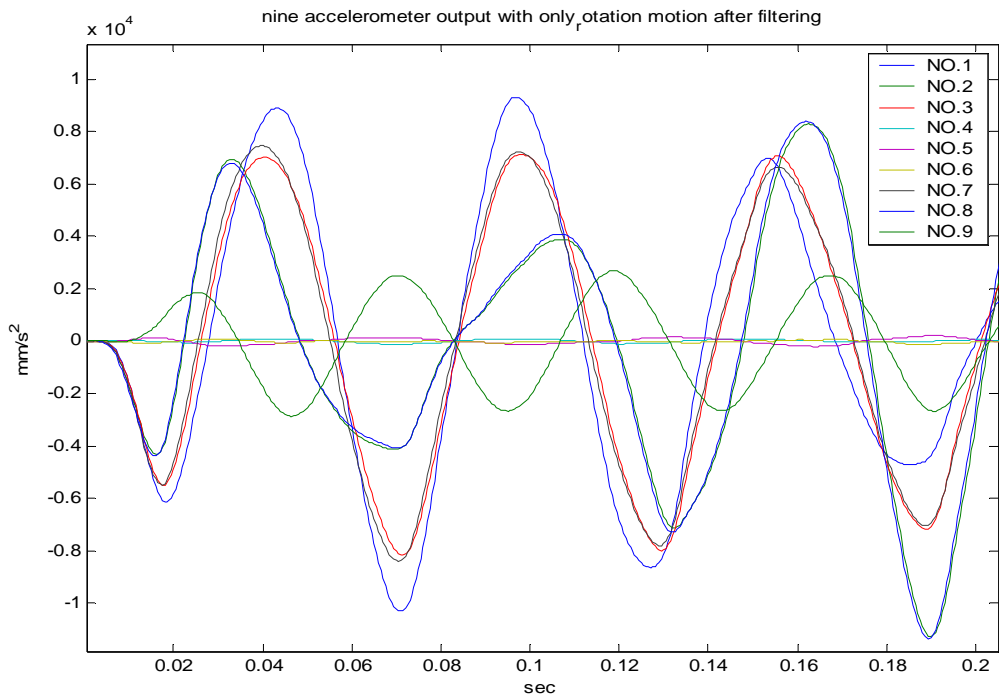


Fig.4.2.3 Signals after Butterworth low-pass filter

Fig.4.2.4 shows the angular rate which is estimated from observer and obtained from differentiating the data of encoder in the rotation frame, Fig.4.2.10 shows that those are in the inertial frame and Fig.4.2.7 shows the Euler' s angular rate. These quantities in X-axis and Y-axis should converge to zero, and in Z-axis should be the sinusoidal wave which is according Eq.4.1. But zero is smaller then resolution in our algorithm, these two curves will not converge to zero. We simulate the same condition as shown in Fig.4.2.5, and angular rate don't converge to zero in X-axis and Y-axis. Because quantity in Z-axis in the rotation frame is equal to it in the inertial frame and $(\phi + \varphi)$, angular displacement can be obtained by integrating from angular rate directly whether it is in the rotation or inertial frame as shown in Fig.4.2.6 and Fig.4.2.11 respectively. Euler' s angular displacement is obtained from solving differential equation (Eq.2.37) directly and shown in Fig.4.2.9. The integral method will accumulate the error and make serious mistake when using Euler' s transform as shown in Fig.4.2.13.

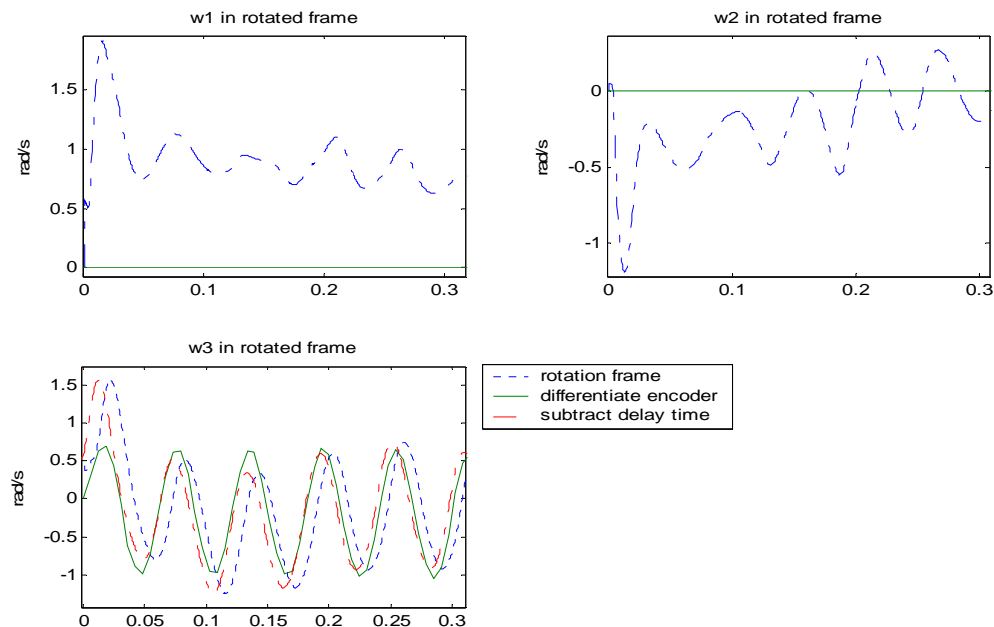


Fig.4.2.4 Angular rate in the rotation frame

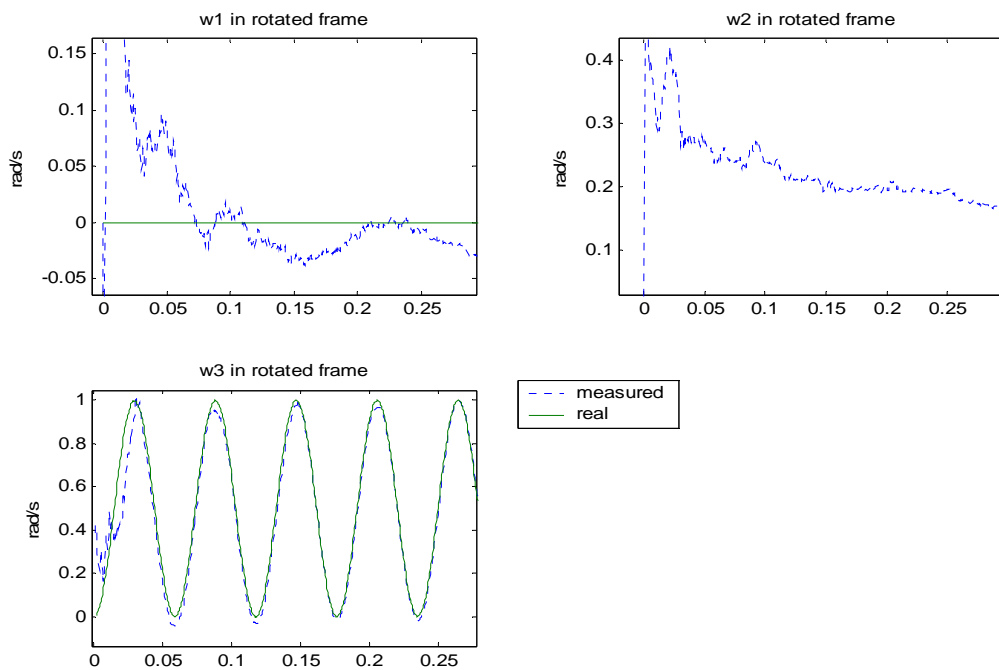


Fig.4.2.5 Angular rate in the rotation frame (simulation)

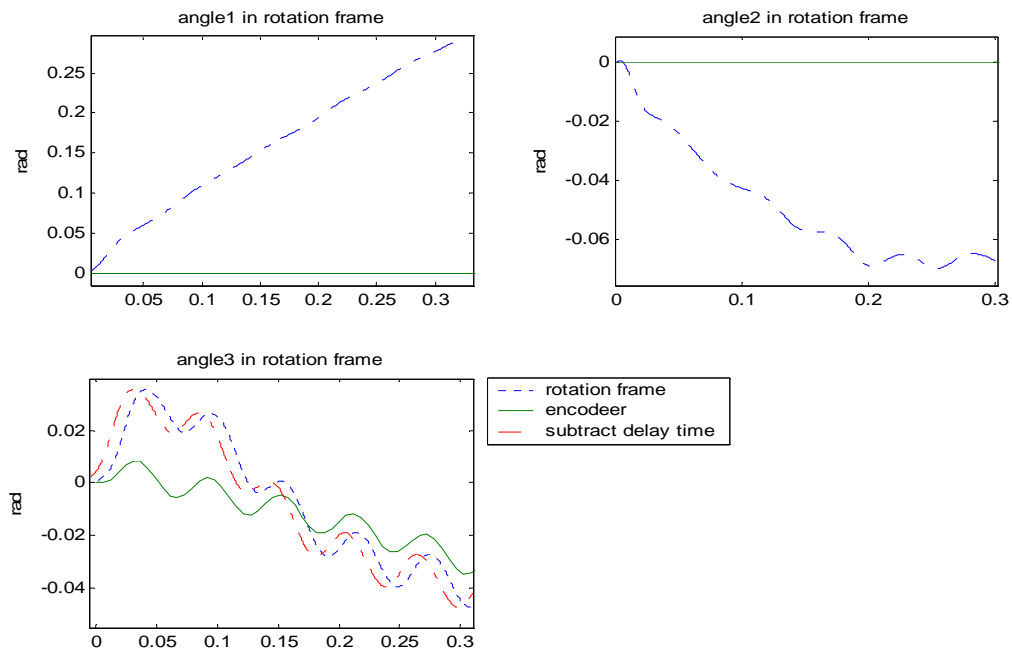


Fig.4.2.6 Angular displacement in the rotation frame

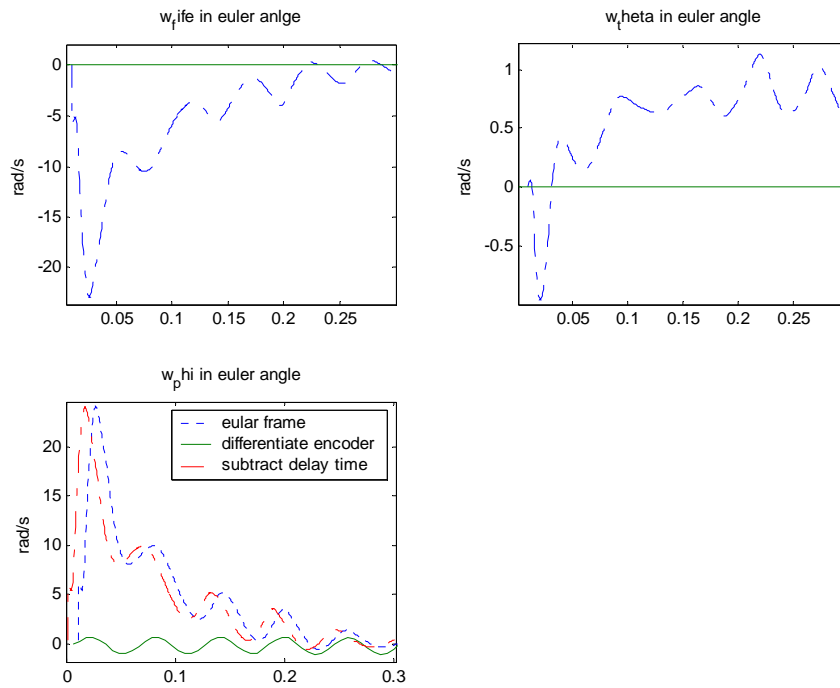


Fig.4.2.7 Euler's angular rate

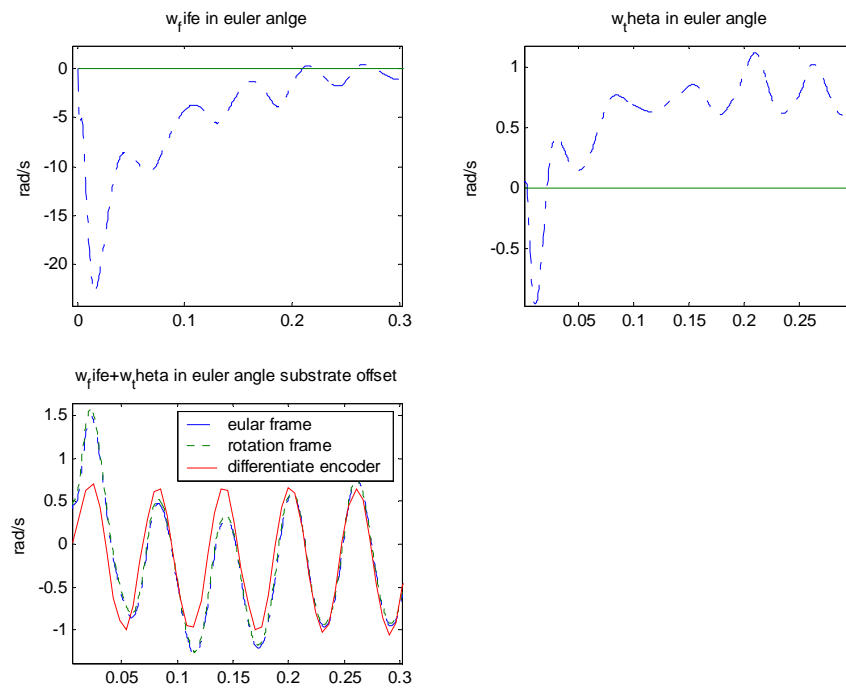


Fig.4.2.8 Euler's angular rate ($(\omega_\phi + \omega_\theta)$ in the third sub-figure)

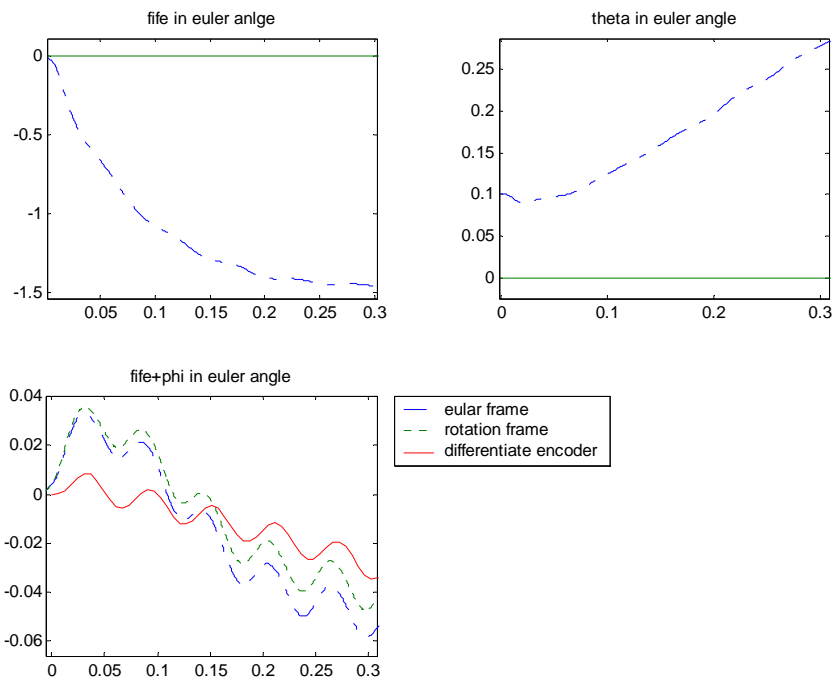


Fig.4.2.9 Euler's angular displacement ($(\phi + \varphi)$ in the third sub-figure)

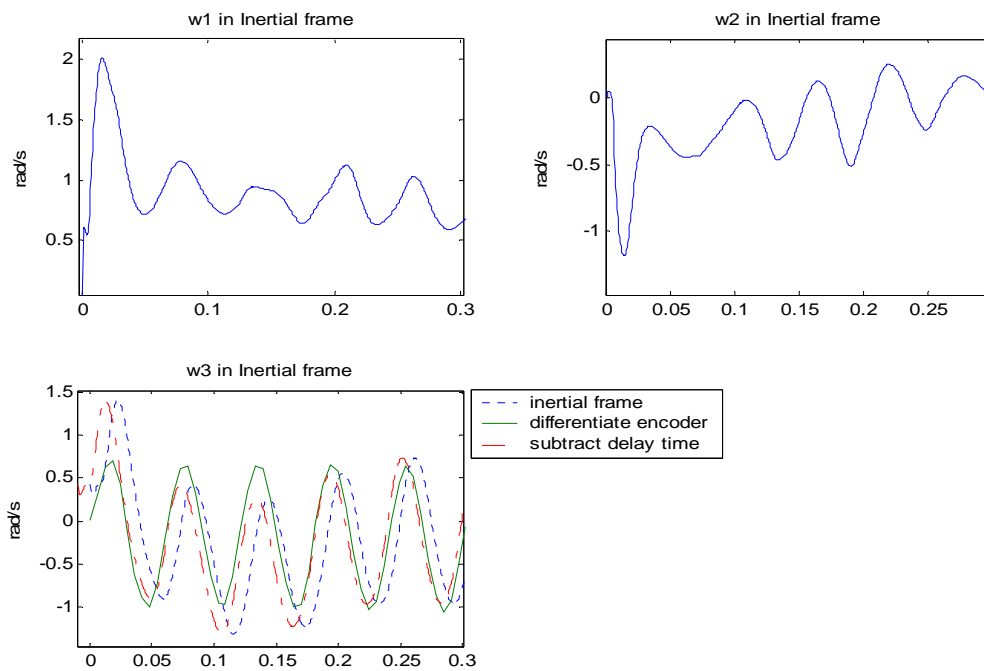


Fig.4.2.10 Angular rate in the inertial frame

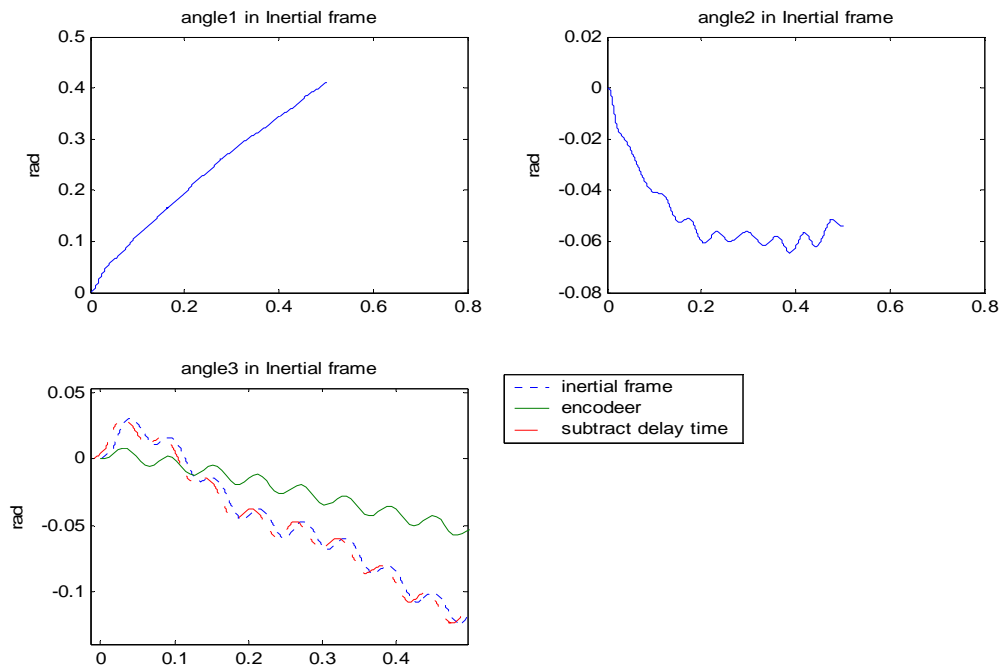


Fig.4.2.11 Angular displacement in the inertial frame

We rewrite Eq.2.6 as Eq.4.6 to obtain linear acceleration in the rotation frame and use Euler's transform (Eq.2.36) to transfer it in the rotation frame into it in the inertial frame Fig.4.2.12 and Fig.4.2.13 indicate the result. With accumulation of the integration error of Euler's angle, acceleration diverges in the Z-axis in the inertial frame. Here, data of encoder is regard as Euler's angle and put it into Eq.2.37 ; and we can get convergent acceleration in the inertial frame by using Euler's angle. Fig.4.2.14 shows the convergent acceleration in the inertial frame.

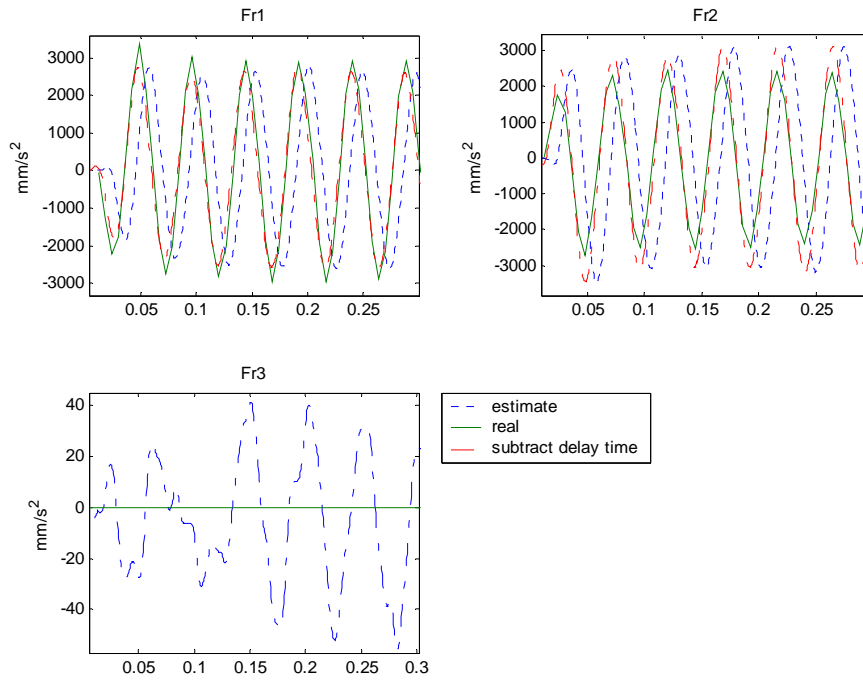


Fig.4.2.12 Linear acceleration in the rotation frame

$$\begin{bmatrix} a_0^b \end{bmatrix} = J^{-1}(4:6,:) \cdot \left(\begin{bmatrix} A_1 \\ A_2 \\ A_3 \\ A_4 \\ A_5 \\ A_6 \end{bmatrix} - \begin{bmatrix} (\bar{n}_1^b)^T \cdot (\bar{\omega}^b \times (\bar{\omega}^b \times \bar{r}_1^b)) \\ (\bar{n}_2^b)^T \cdot (\bar{\omega}^b \times (\bar{\omega}^b \times \bar{r}_2^b)) \\ (\bar{n}_3^b)^T \cdot (\bar{\omega}^b \times (\bar{\omega}^b \times \bar{r}_3^b)) \\ (\bar{n}_4^b)^T \cdot (\bar{\omega}^b \times (\bar{\omega}^b \times \bar{r}_4^b)) \\ (\bar{n}_5^b)^T \cdot (\bar{\omega}^b \times (\bar{\omega}^b \times \bar{r}_5^b)) \\ (\bar{n}_6^b)^T \cdot (\bar{\omega}^b \times (\bar{\omega}^b \times \bar{r}_6^b)) \end{bmatrix} \right) \quad (4.6)$$

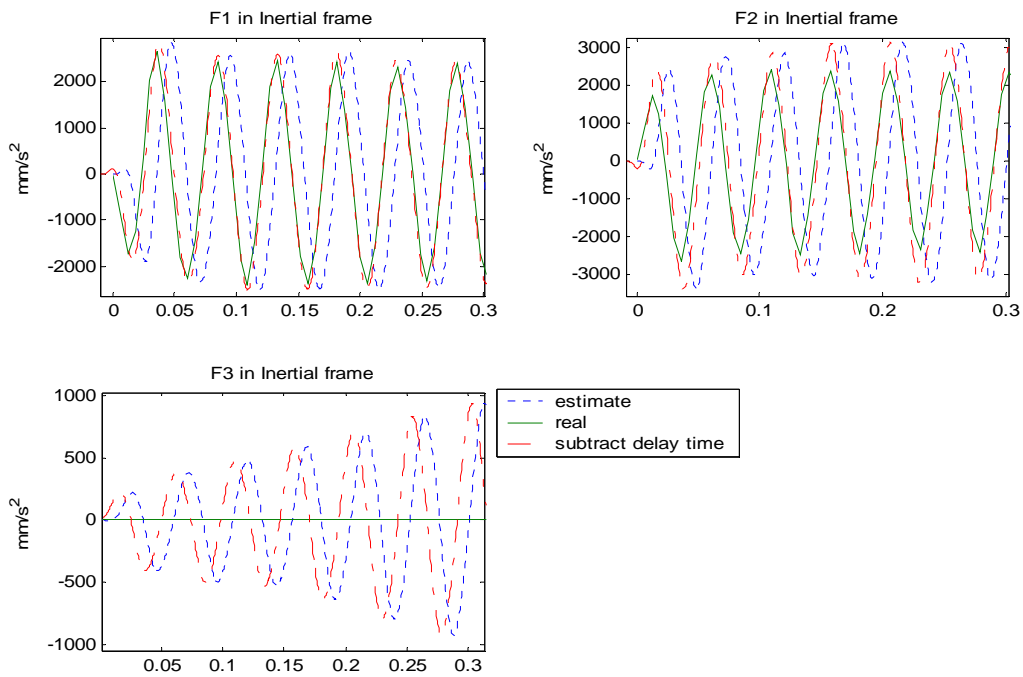


Fig.4.2.13 Linear acceleration in the inertial frame

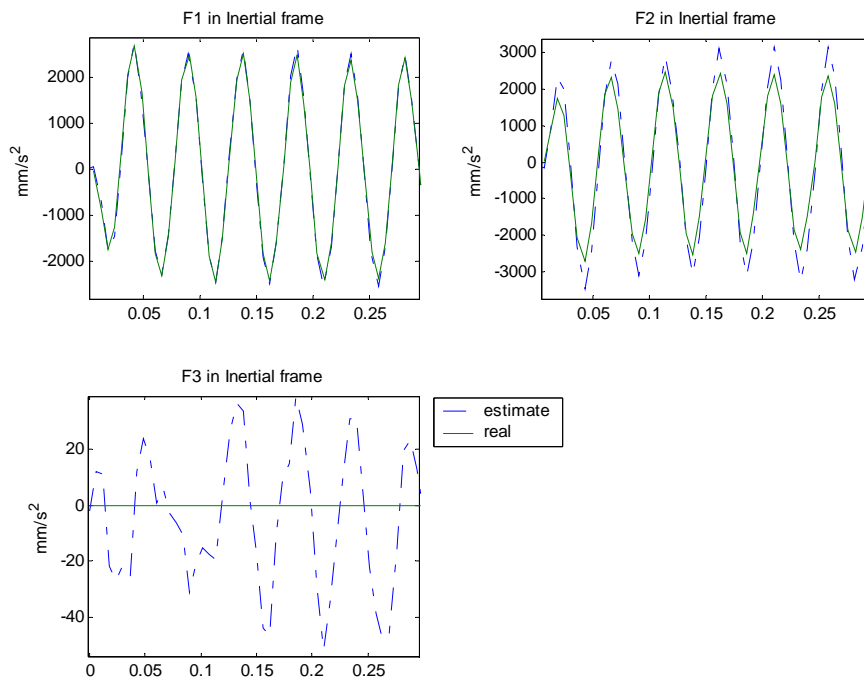


Fig.4.2.14 Linear acceleration in the inertial frame (with encoder information)

4.3 Z-axis rotation with biaxial linear acceleration and non-zero initial condition



Fig4.3.1 Experimental set up

The difference between this experiment and the above experiment is initial condition of angle of Y-axis and Z-axis as shown in Fig.4.3.1, angle of Y axis is 90 degree and Z axis is -90 degree as shown in Fig.4.3.1. Fig.4.3.1 presents the set up of this experiment. Because initial condition in Y axis is not zero, equ.2.35 can not be rewritten as equ.4.5. Quantities of Y axis and Z axis in the rotation frame are similar to -X axis and -Y axis in the inertial frame respectively when φ is still changed small enough. Quantities of X axis in the rotation frame are equal to Z axis in the inertial frame. The influence of acceleration of gravity on each accelerometer is time-varying, so we should separate acceleration of gravity from accelerometer output. This result is shown in Fig4.3.8~Fig4.3.10.

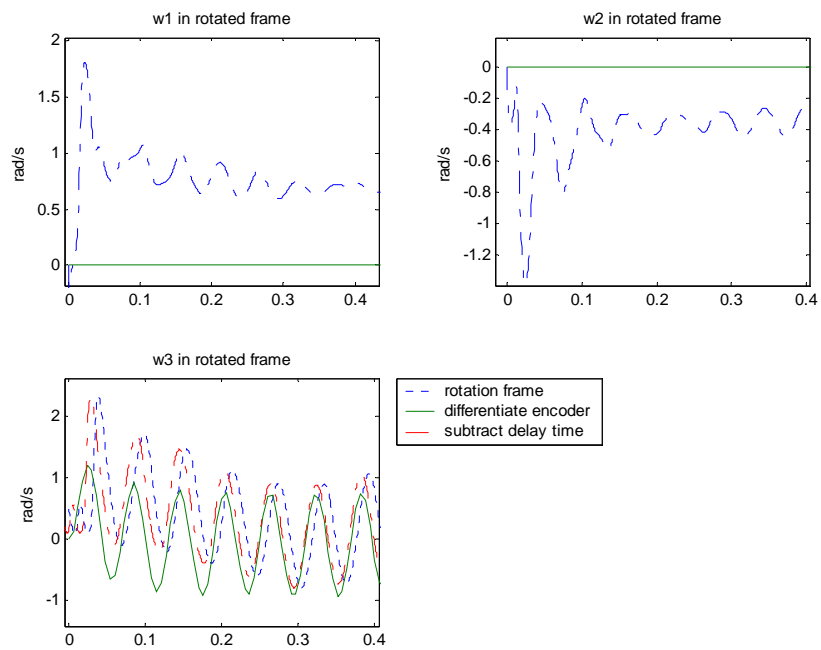


Fig4.3.2 Angular rate in the rotation frame

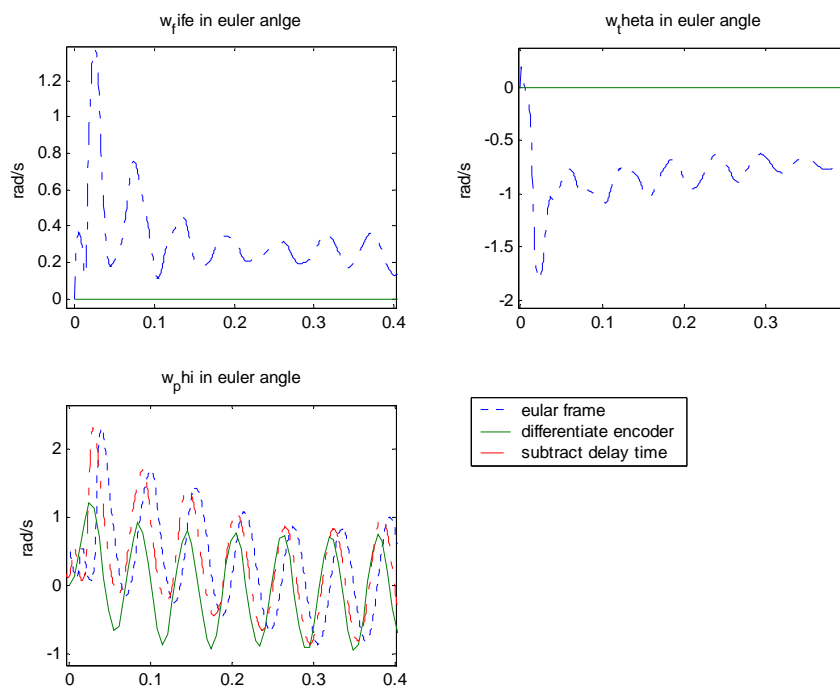


Fig4.3.3 Euler's angular rate

Algorithm flow (Fig.4.2.2) indicated that the influence of integral error of Euler's angle on linear acceleration in the inertial frame is the most serious. Because linear acceleration in the rotation frame is obtained by Eq.4.6 and it carry about a lot of white noise, it is inaccuracy when we transfer it into linear acceleration in the inertial frame with Euler's angle. There is the same circumstance when we transfer the angular rate in the rotation frame into it in the inertial frame. The angular rate in the rotation frame is obtained by Iterated Extended Kalman filter without white noise, so it is more accuracy than linear acceleration. In this experiment, because the angular rate in the rotation frame converges after 0.3 second, the angular rate in the inertial frame is divergent shown as Fig4.3.4 and Fig.4.3.6. If accuracy Euler's angle as encoder information is being substituted Euler's angle calculated by Eq.2.37 shown as Fig.4.3.5 and Fig.4.3.7, the angular rate will not be divergence in X-axis in the inertial frame. Fig.4.3.4 and Fig.4.3.5 show the angular rate between 0 and 0.4 second, Fig.4.3.6 and Fig.4.3.7 show the angular rate between 0 and 4 second.

Linear acceleration in the inertial frame is also divergence as the above experiment. Encoder information is being substituted Euler's angle shown to obtained linear acceleration in the inertial frame as Fig.4.3.10. Fig.4.3.8 presents linear acceleration in the rotation frame and Fig.4.3.9 shows linear acceleration transferred by Euler's angle which is calculated by Eq.2.37 in the rotation frame and it will be divergence.

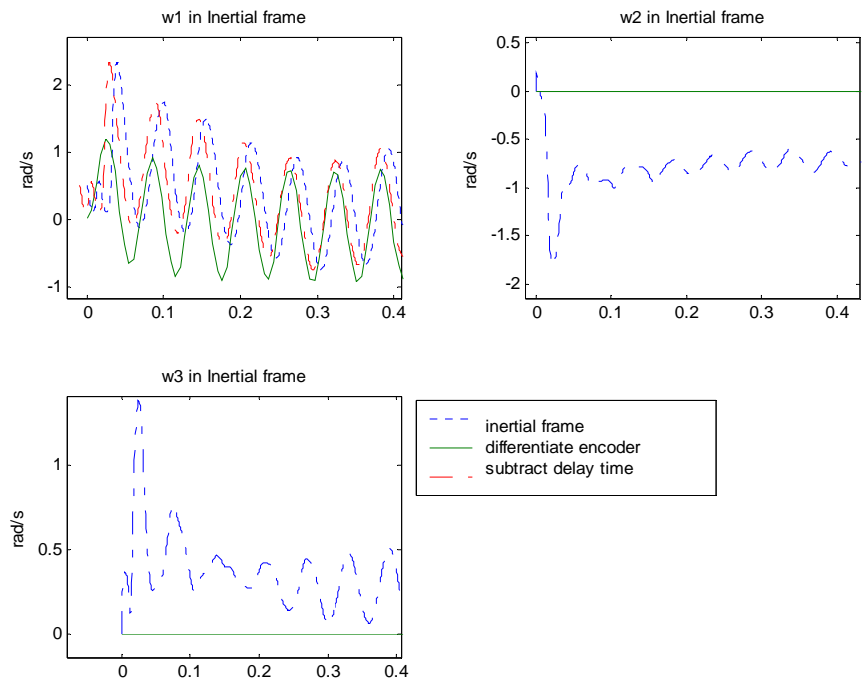


Fig4.3.4 Angular rate in the inertial frame

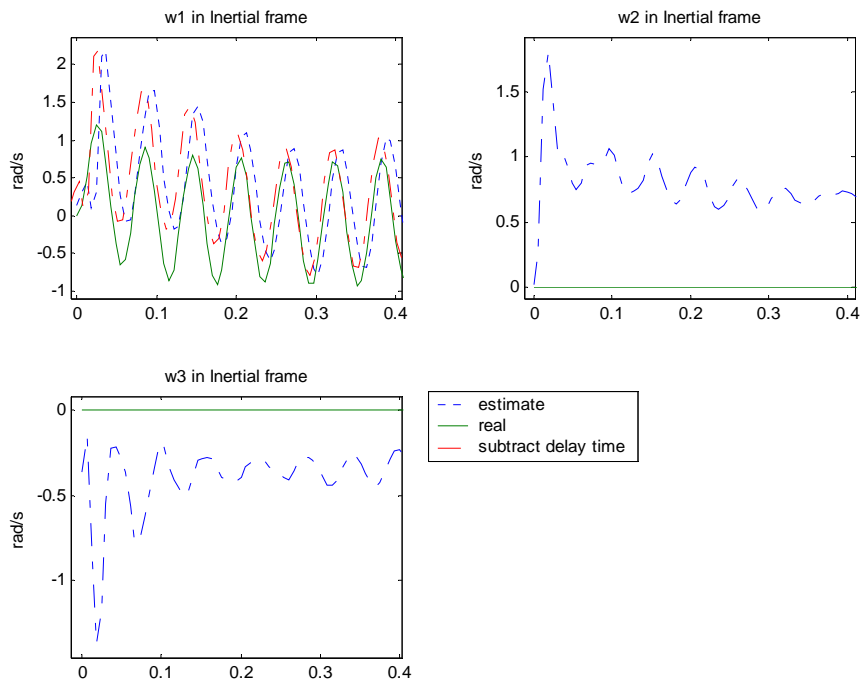


Fig4.3.5 Angular rate in the inertial frame (with encoder information)

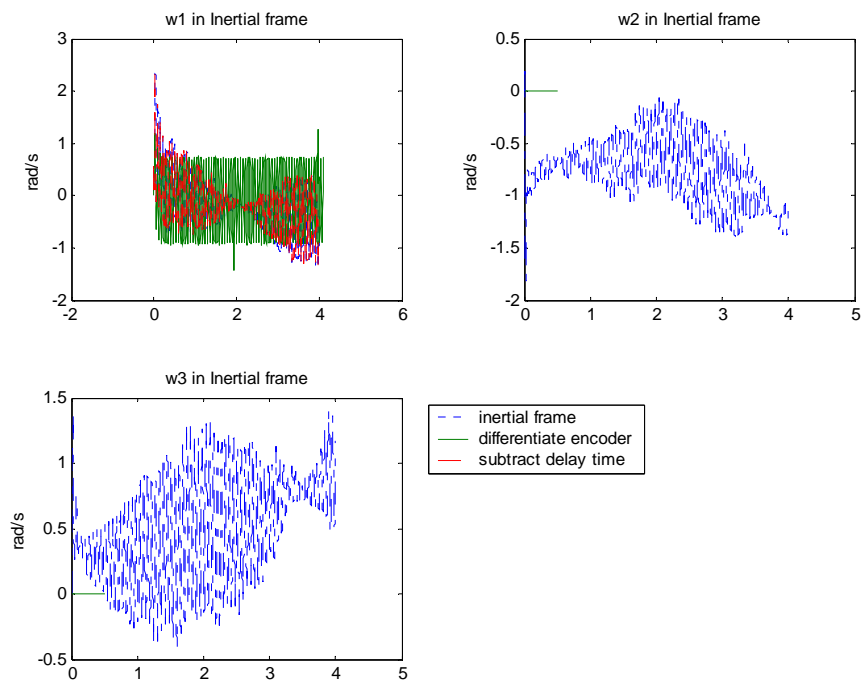


Fig4.3.6 Angular rate in the inertial frame (with encoder information)

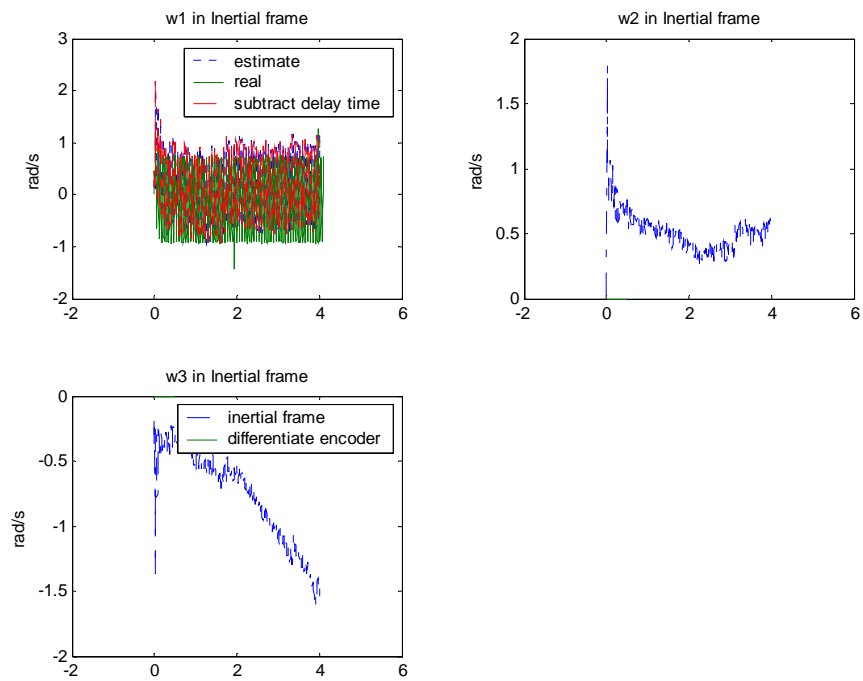


Fig4.3.7 Angular rate in the inertial frame (with encoder information)

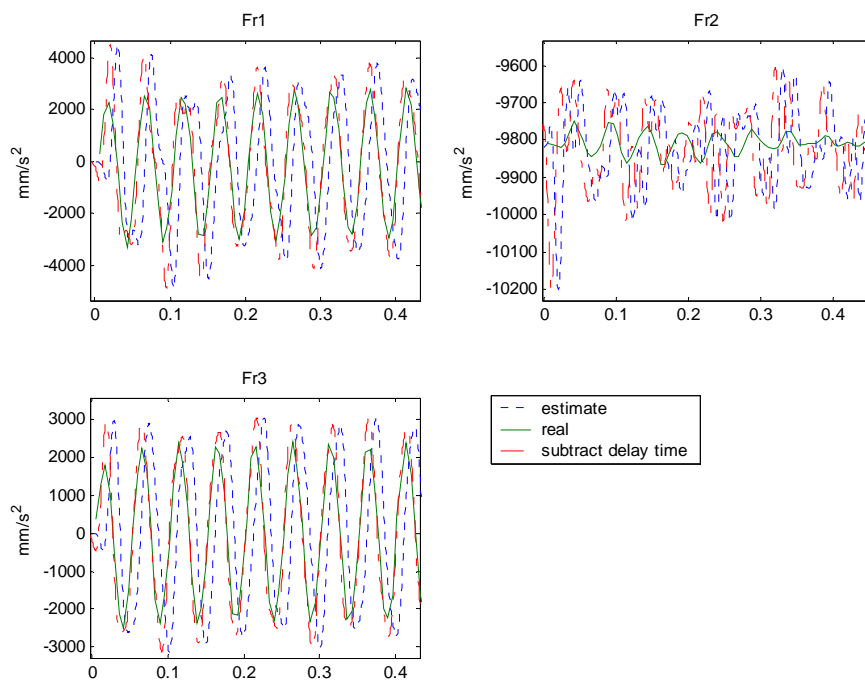


Fig4.3.8 Linear acceleration in the rotation frame

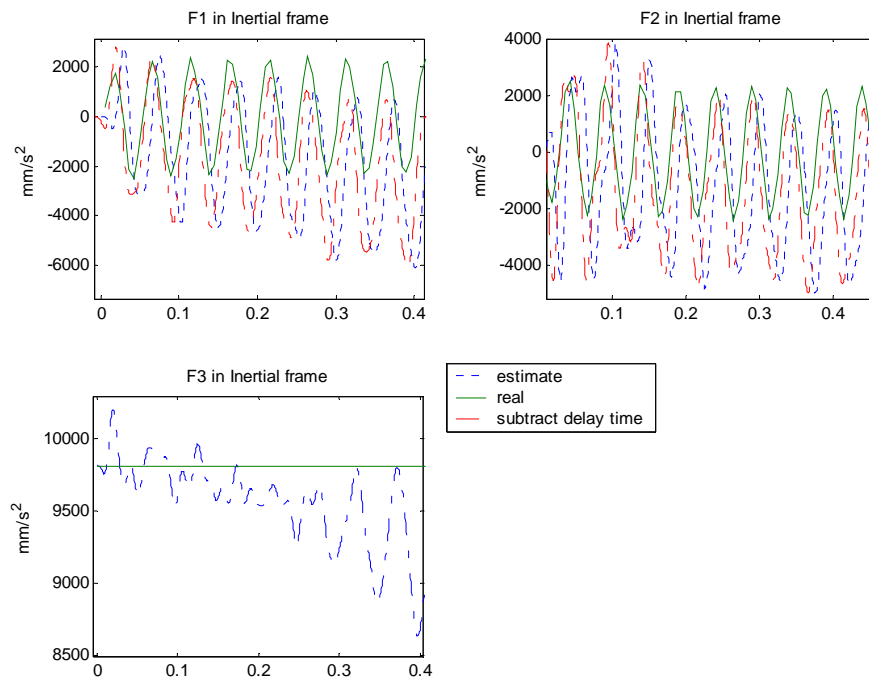


Fig4.3.9 Linear acceleration in the inertial frame

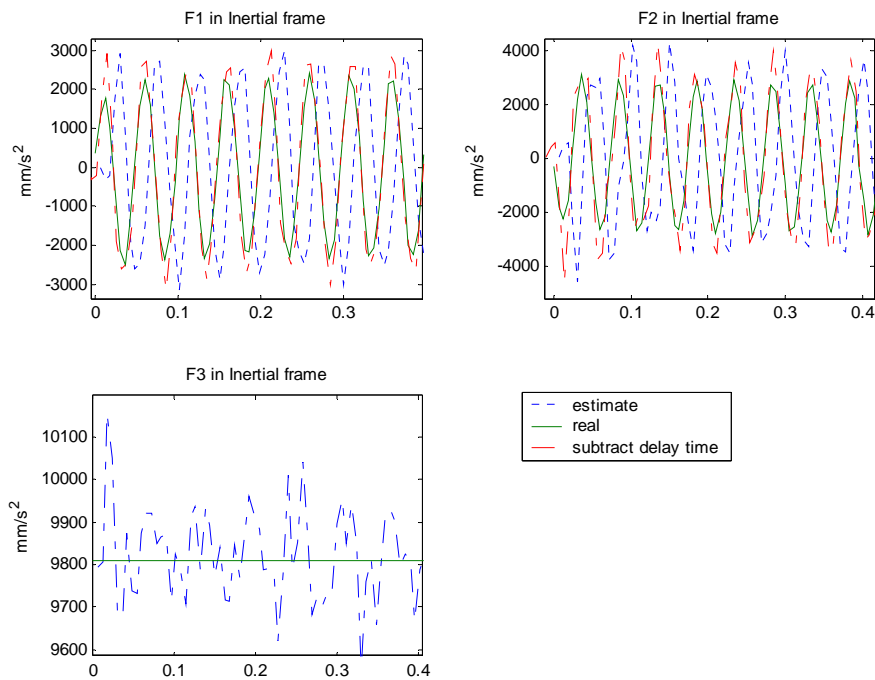


Fig4.3.10 Linear acceleration in the inertial frame (with encoder information)

4.4 Y-axis rotation with biaxial linear acceleration

The difference between this experiment and the above experiments is initial condition and the rotational axis. Initial condition of angle is zero whether it is in any axes and the axis of rotation is parallel to Y axis in the rotation frame shown in Fig.4.4.1. We rewrite Eq.2.36 as Eq.4.7 with these initial conditions. According to Eq.4.7, quantities in the Euler's angle θ are the same as quantities of Y axis in the rotation or inertial frame. Fig.4.4.2, Fig.4.4.6 and Fig.4.4.4 show the angular rate in the rotation frame, inertial frame and Euler's angular rate respectively, there are only sine wave in the Y axis whether the quantities are shown in any Figure.

$$\begin{aligned}
& \varphi = 0 \quad \dot{\varphi} = 0 \\
& X^i = \begin{bmatrix} \cos \varphi & -\sin \varphi & 0 \\ \sin \varphi & \cos \varphi & 0 \\ 0 & 0 & 1 \end{bmatrix} \begin{bmatrix} \cos \theta & 0 & \sin \theta \\ 0 & 1 & 0 \\ -\sin \theta & 0 & \cos \theta \end{bmatrix} \begin{bmatrix} \cos \varphi & -\sin \varphi & 0 \\ \sin \varphi & \cos \varphi & 0 \\ 0 & 0 & 1 \end{bmatrix} X^b \\
& = \begin{bmatrix} \cos \theta & 0 & \sin \theta \\ 0 & 1 & 0 \\ -\sin \theta & 0 & \cos \theta \end{bmatrix} X^b
\end{aligned} \tag{4.7}$$

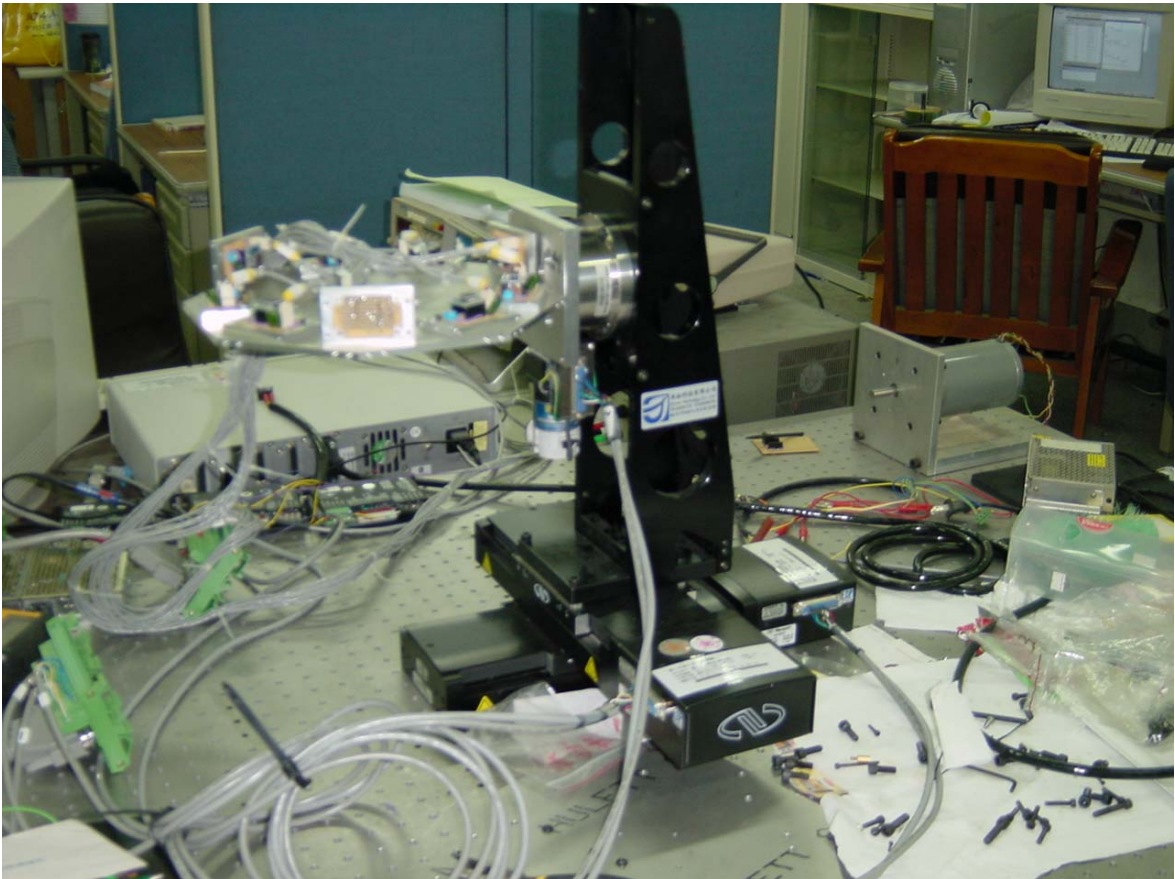


Fig4.4.1 Experimental set up

Because accumulation of integral error is more serious in this experiment, Euler's angular rate which is calculated by Eq.2.37 is divergent. We transfer quantities (angular rate or linear acceleration) in the rotation frame into inertial frame and those are divergent more easily in the inertial frame. Accuracy Euler's angle as encoder information is substituted Euler's angle calculated by Eq.2.37 shown as Fig.4.4.3, Fig.4.4.5 and Fig.4.4.8,

the angular rate in the inertial frame, Euler's angular rate and linear acceleration in the inertial frame will not be divergence in Y-axis.

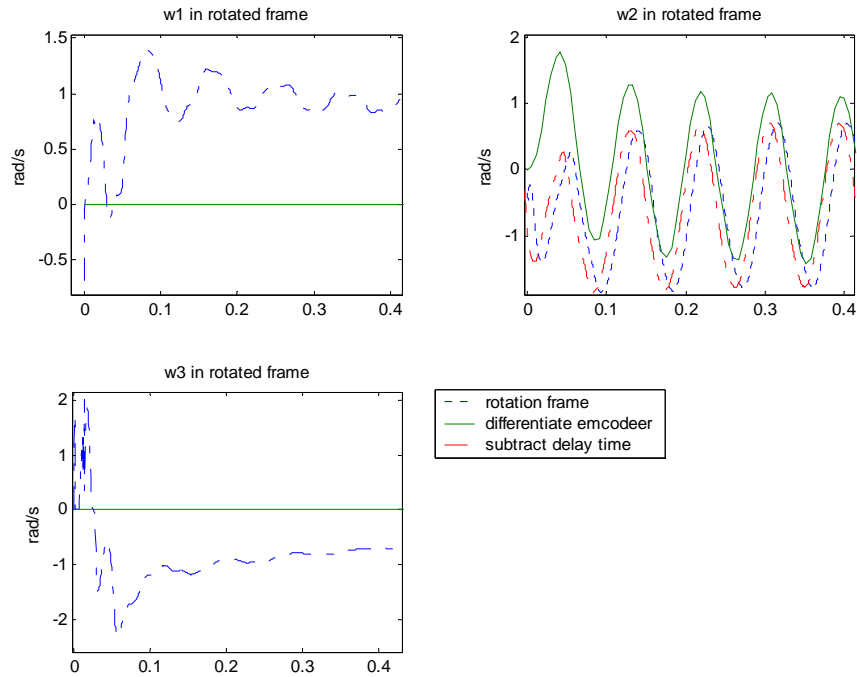


Fig.4.4.2 Angular rate in the rotation frame

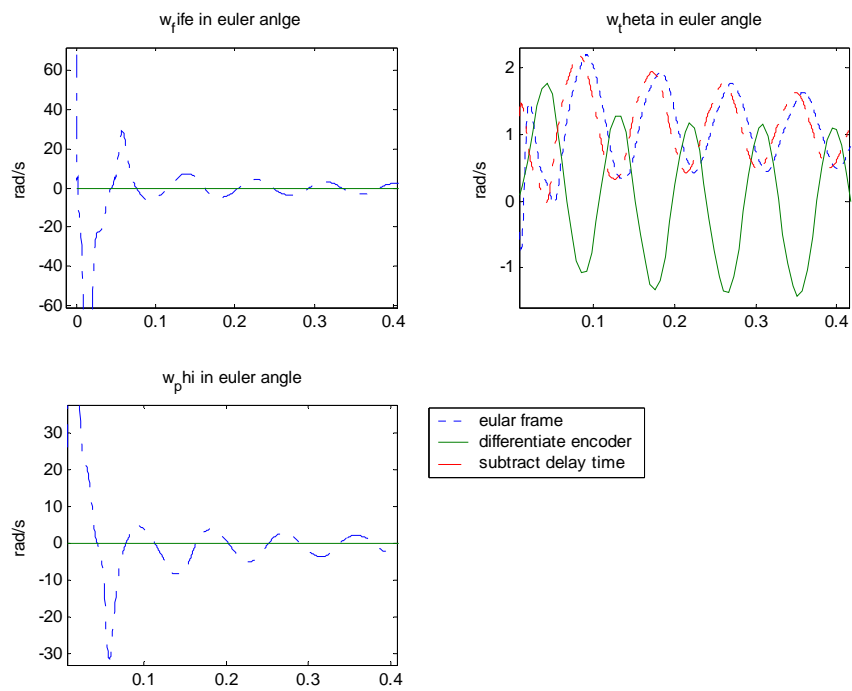


Fig.4.4.3 Euler's angular rate

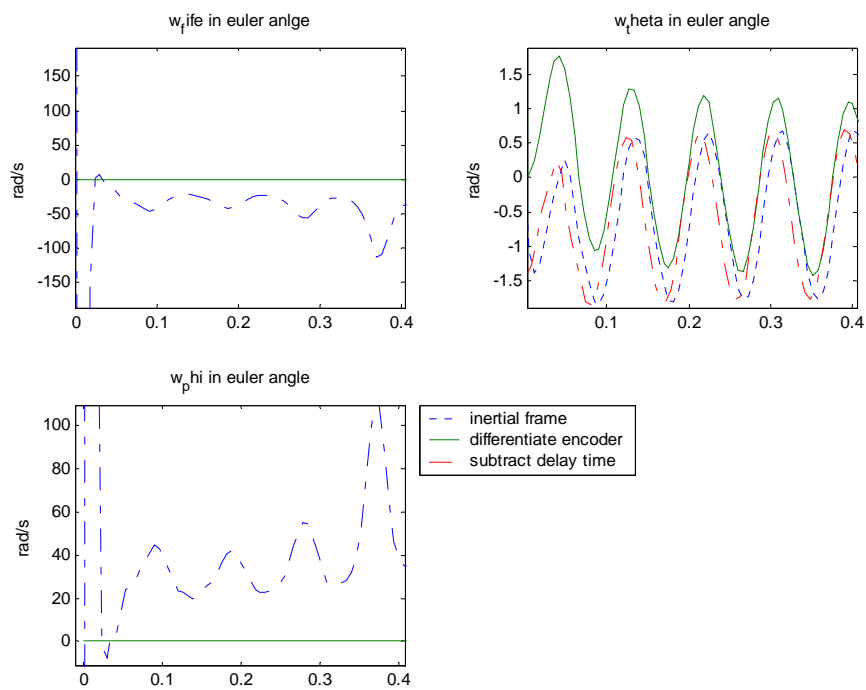


Fig.4.4.4 Euler's angular rate (with encoder information)

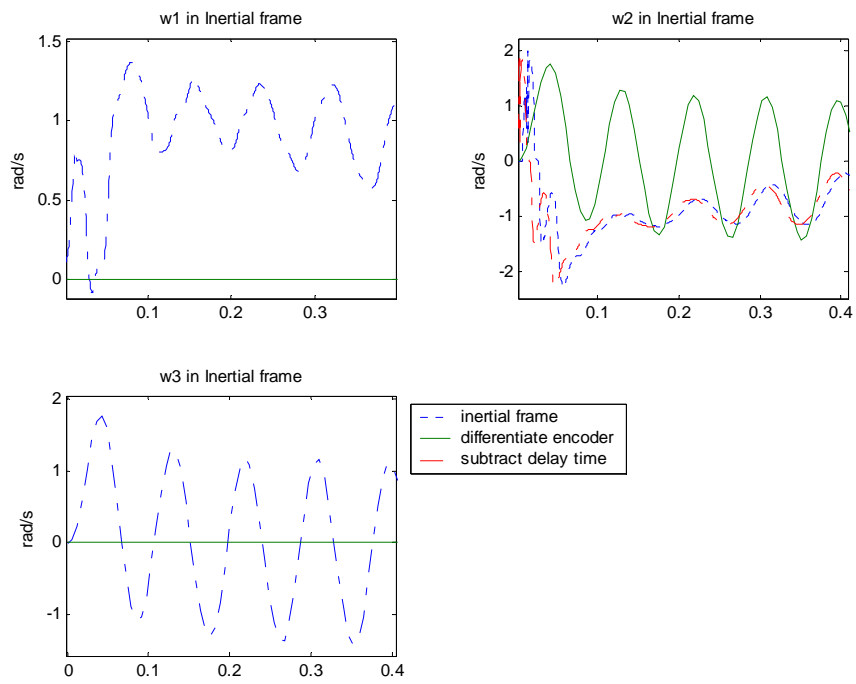


Fig.4.4.5 Angular rate in the inertial frame

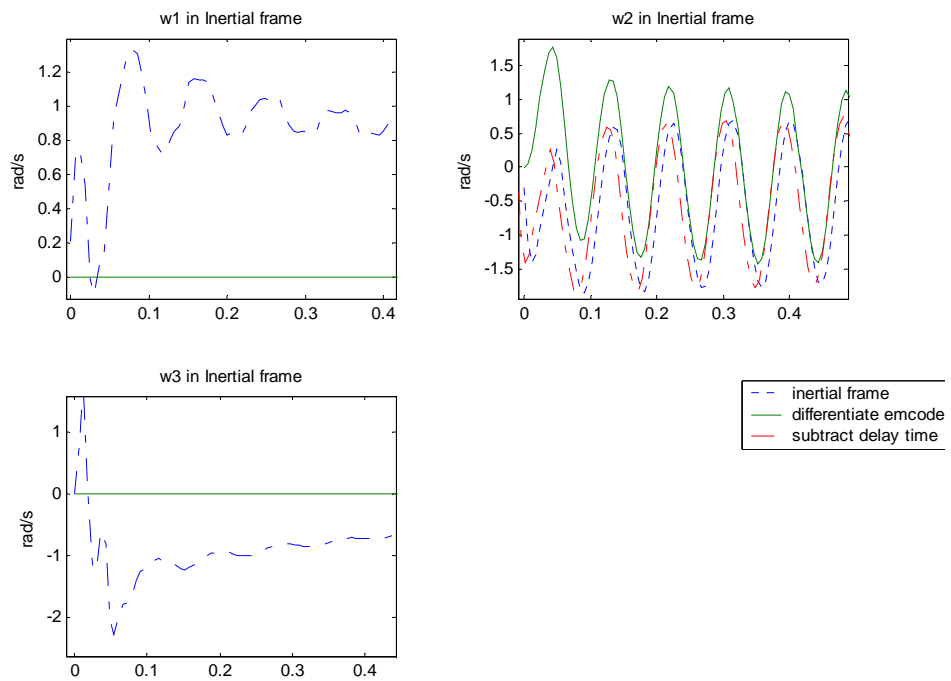


Fig.4.4.6 Angular rate in the inertial frame (with encoder information)

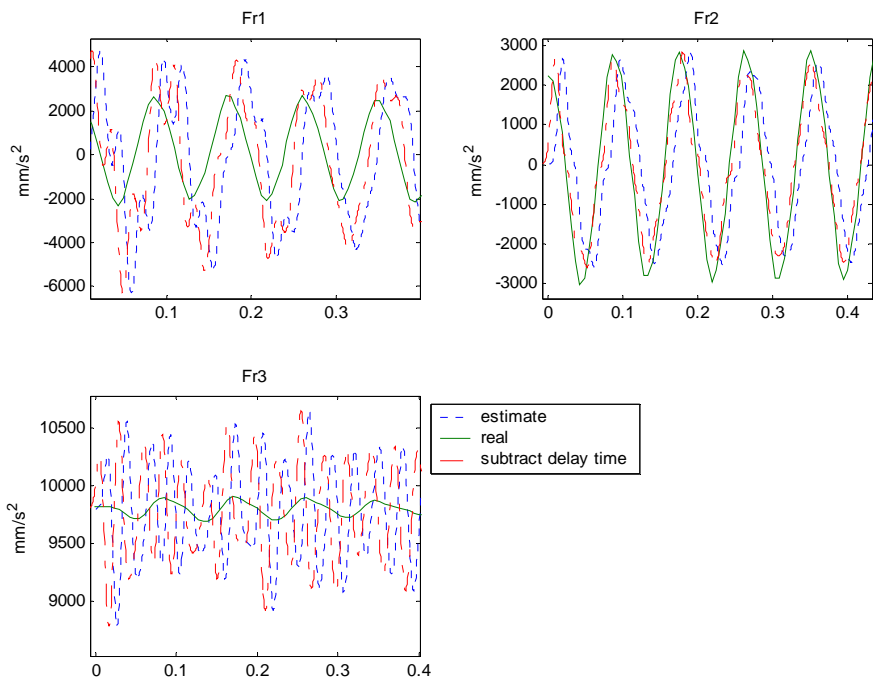


Fig.4.4.7 Linear acceleration in the rotation frame

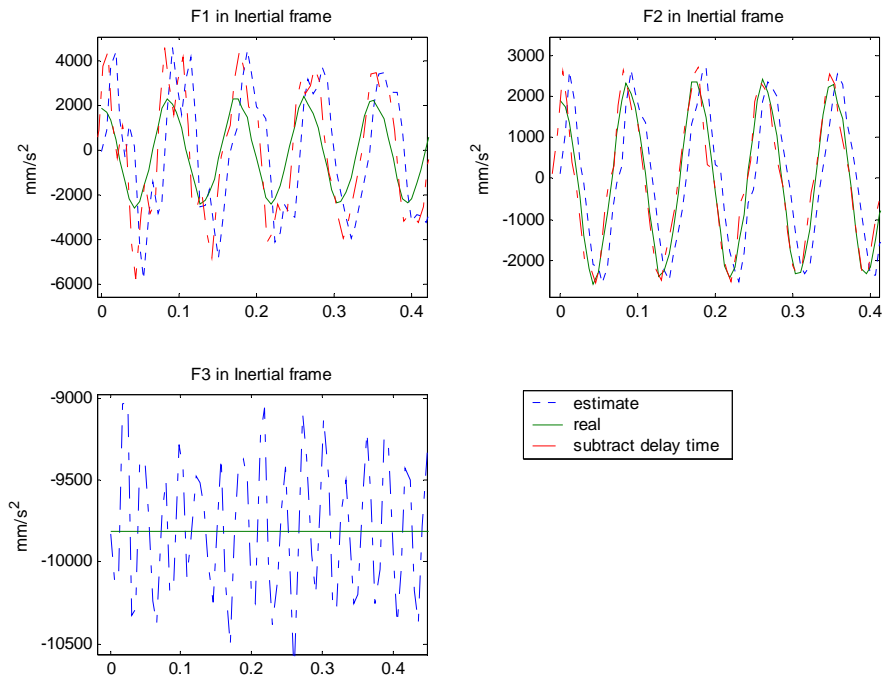


Fig.4.4.8 Linear acceleration in the inertial frame (with encoder information)

4.5 Discussion

The uncertainties of experiment scheme may cause the difference between information from encoder and states of algorithm. The discussion of experimental error below will be shown to emphasize the importance of three features; linear vibration of the optical table, rotational vibration of the optical table and DC-drift of accelerometer output or other noise.

Linear vibrations of the optical table

The first question to be discussed is linear vibration of the optical table. Fig4.5.1 illustrates that the frequency of linear vibration is the same as the motion in the experiment. Amplitude of this vibration is almost 200mm/s^2 in the X-axis and Y-axis, and 50mm/s^2 in the Z-axis as shown in Fig.4.5.2. According these conditions, we simulate how this error influences physical quantities in our algorithm.

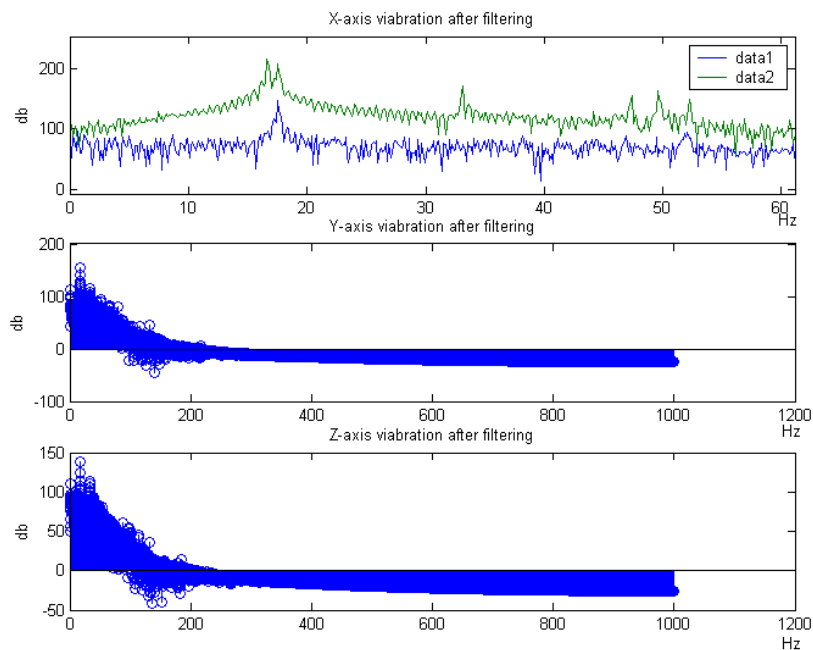


Fig.4.5.1 Vibration of tri-axes in the frequency domain

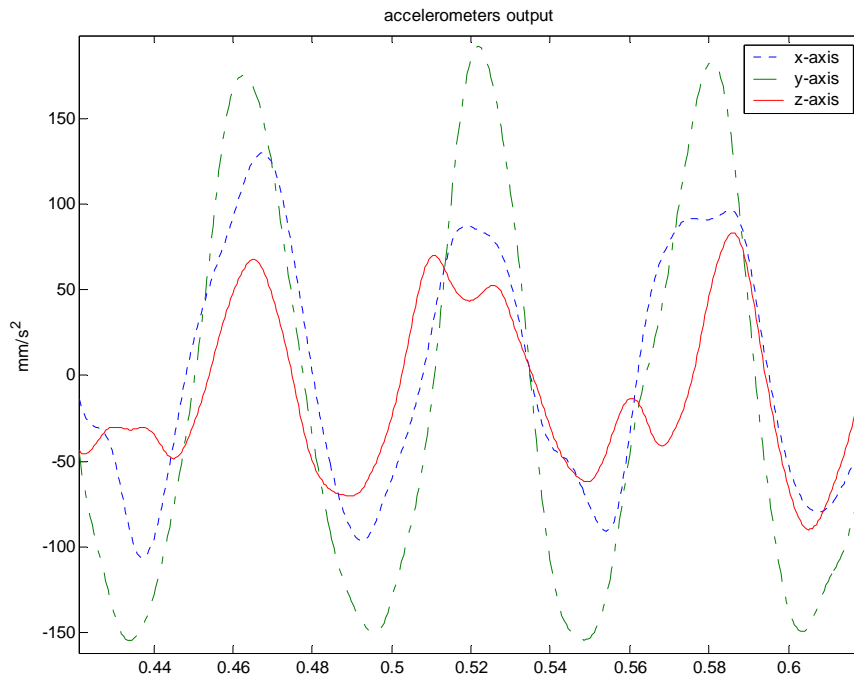


Fig.4.5.2 Vibration of tri-axes

Fig.4.5.3 shows that the vibration makes converging rate of the angular rate to be slow, but it does not change the accuracy when it converges. The amplitude will increase by 200mm/s^2 in the X-axis and Y-axis, as shown in the Fig.4.5.4. It follows from what has been said that the error of linear vibration affects only the accuracy in the linear acceleration and converging rate of the angular rate in the rotation frame.

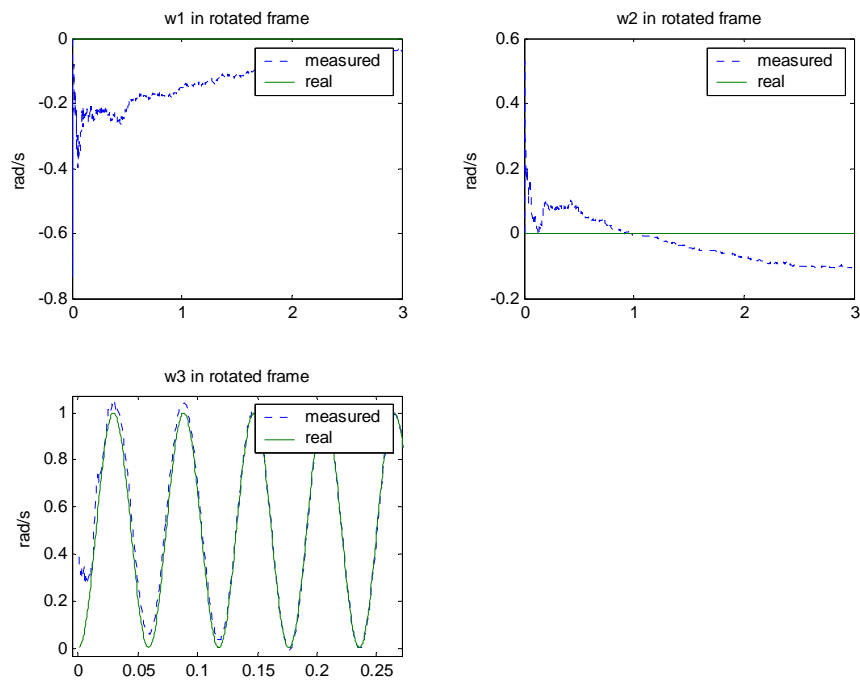


Fig.4.5.3 Angular rate in the rotation frame (with linear vibration)

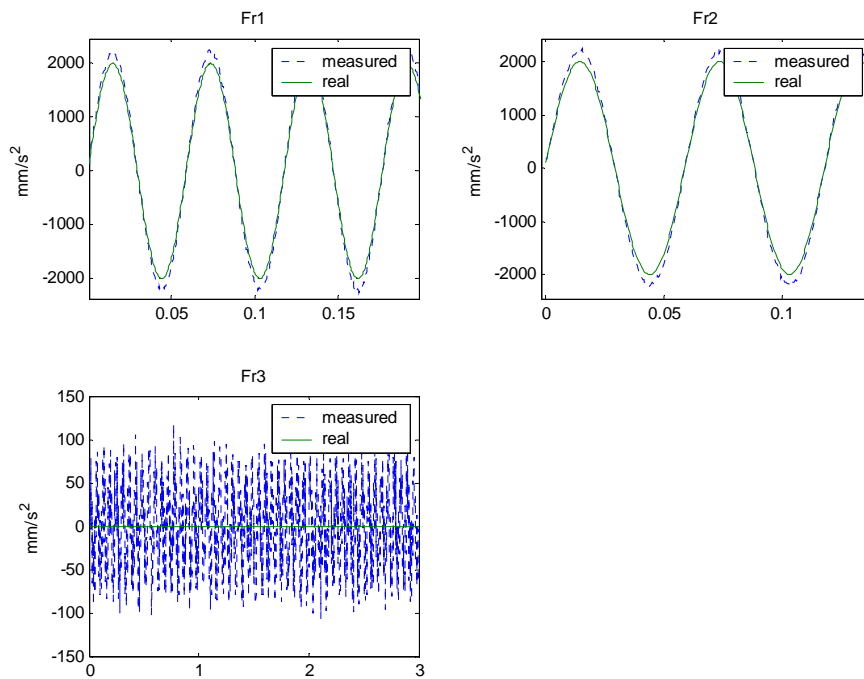


Fig.4.5.4 Linear accelerations in the rotation frame (with linear vibration)

Rotational vibration of the optical table

Because the angular rate can not be sensed by our experiments, we just discuss this question without experimental verification. We assumed that frequency of rotational vibration is equal to actual motion and the amplitude is about 0.1rad/s^2 . Fig.4.5.5 and Fig.4.5.6 show that the result of this simulation is contrary to the above simulation. Rotational vibration affects the accuracy of angular rate in the rotation frame and it doesn't affect linear acceleration. The influence is the same to rotational vibration we designed. Thus, we see that linear vibration affects linear acceleration and rotational vibration affects angular rate respectively.

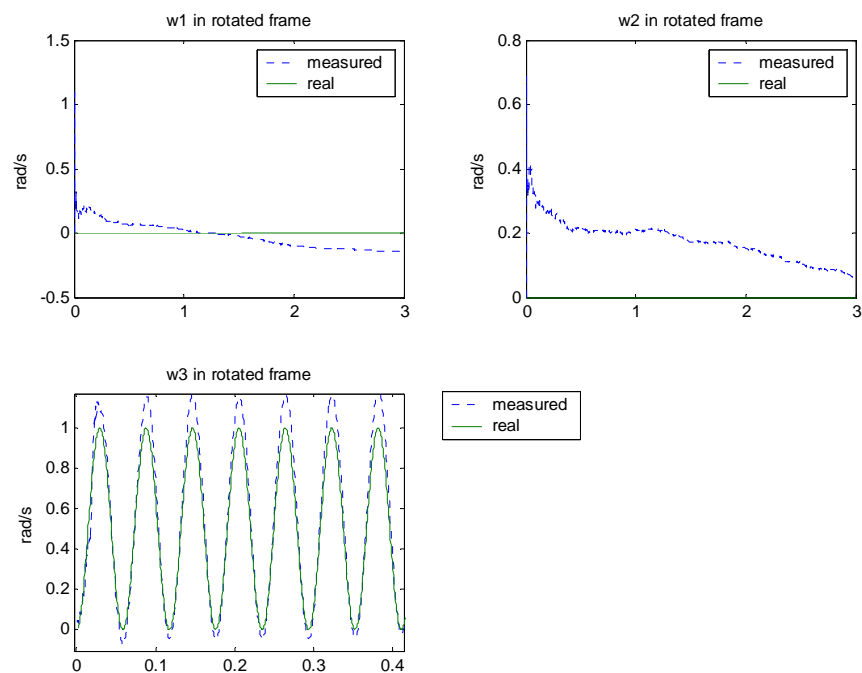


Fig.4.5.5 Angular rate in the rotation frame (with rotational vibration)

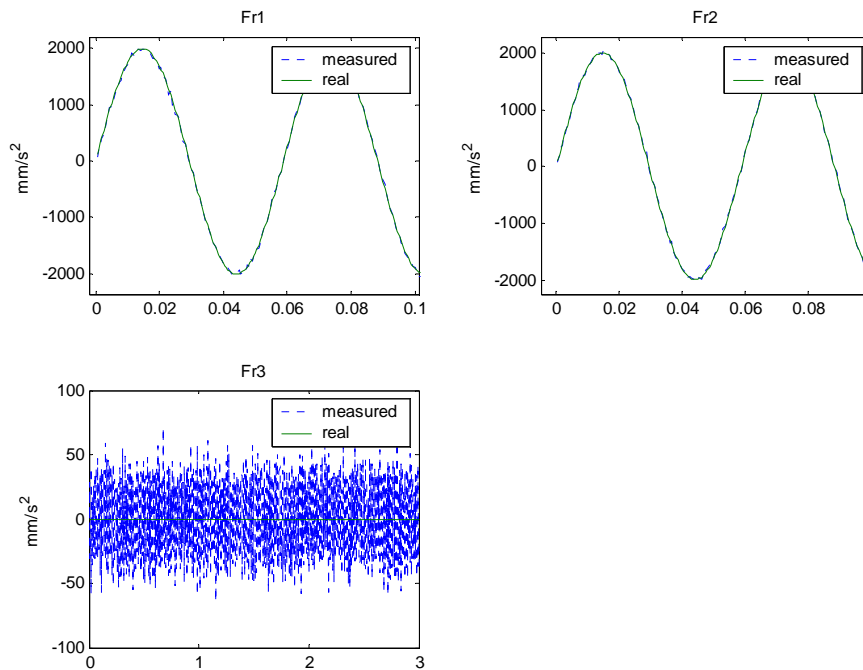


Fig.4.5.6 Linear accelerations in the rotation frame (with rotational vibration)

DC-drift or other noise

We assumed that there is 5Hz, 100mm/s² DC-drift in the nine output signals of accelerometers. Fig.4.5.7 gives a good account of the most serious error in transient time. To put it more precisely, DC-drift affects the converging rate more seriously than we discussed above. This kind of error doesn't affect linear acceleration seriously, as shown in Fig.4.5.8. Fig.4.5.9 shows that the influence of random frequency (1~17HZ) of other noises (backlash of screw, vibration of stage and etc.) on converging rate of angular rate in the rotation frame has slight variations in this two simulations. Fig.4.5.10 shows that the influence on linear acceleration in the rotation frame is very slight. We can not say for certain whether this condition (frequency and amplitude) is fit or not, but we can know that these errors affect the convergent rate more seriously than what we discussed above.

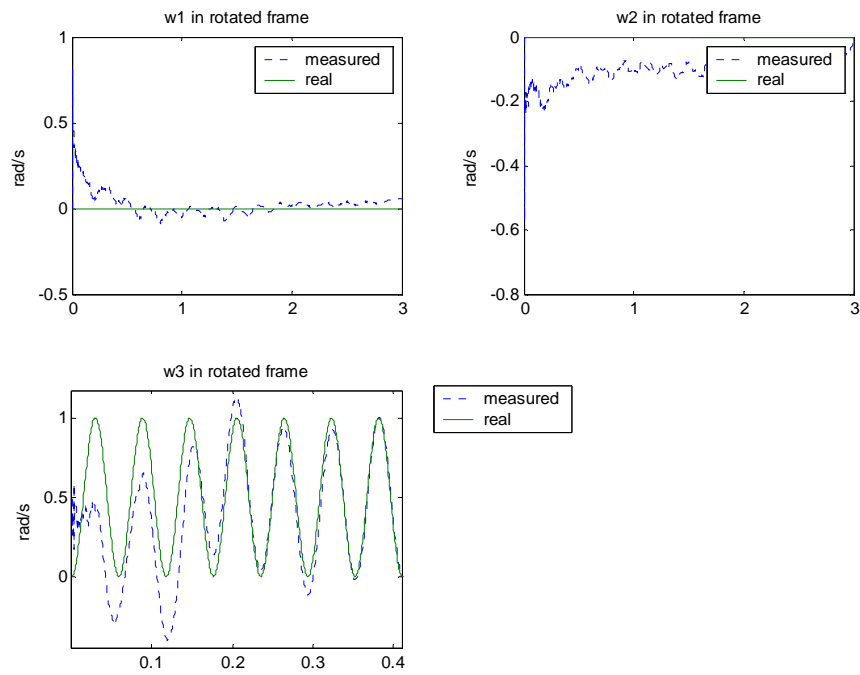


Fig.4.5.7 Angular rate in the rotation frame (with 5Hz 100mm/s² DC-drift)

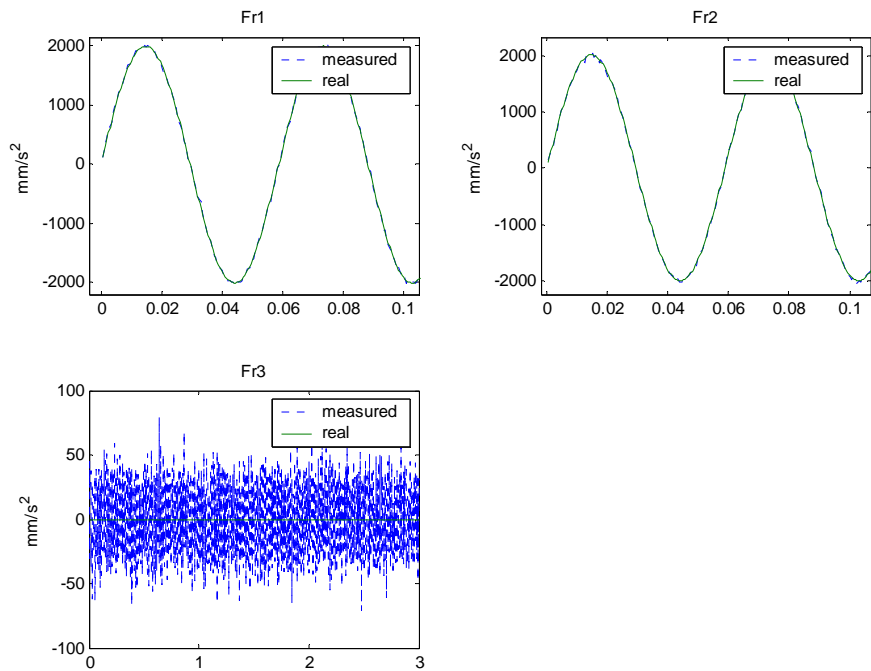


Fig.4.5.8 Linear accelerations in the rotation frame (with 5Hz 100mm/s² DC-drift)

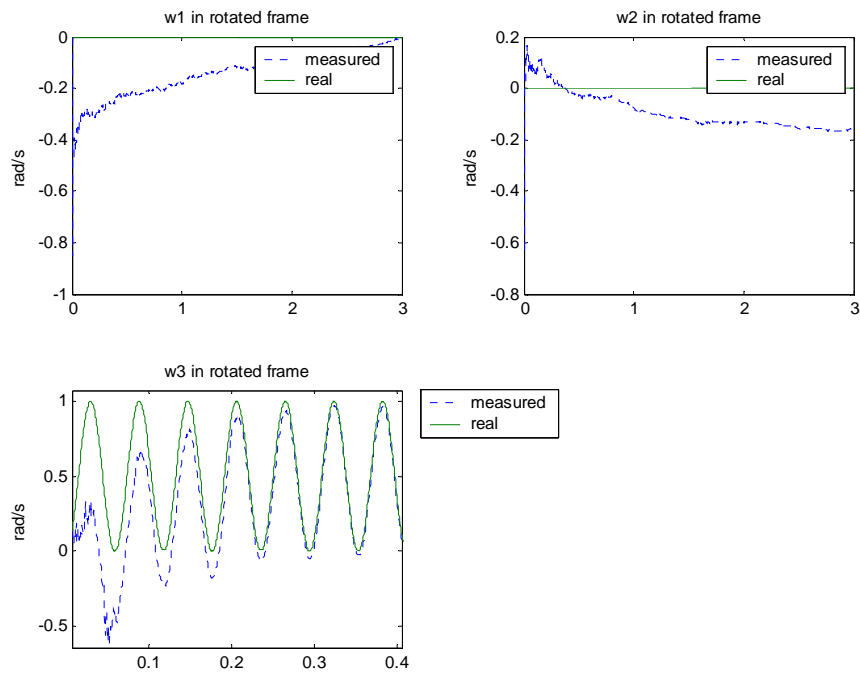


Fig.4.5.9 Angular rate in the rotation frame (with 1~17Hz 100mm/s² other noise)

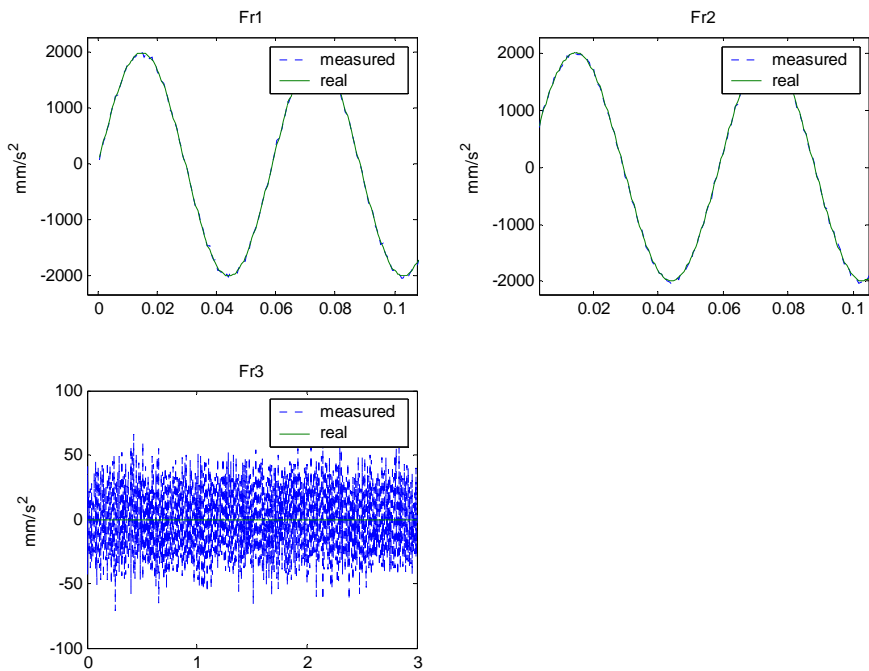


Fig.4.5.10 Linear accelerations in the rotation frame (with 5Hz 100mm/s² other noise)

According to Fig.4.1.2, the experiments error influence directly converging rate and resolution of angular rate, and resolution of linear acceleration in the rotation frame. It follows from what has been said that linear vibration affects linear acceleration, rotational vibration affects angular rate and DC-drift or other noises affect the converging rate more seriously than that we discuss above.



CHAPTER 5

CONCLUSION AND FUTURE WORKS

5.1 Conclusion

The observer-based planar Gyro-free IMU has been proven to be feasible for deriving position information (angular acceleration, angular velocity, linear acceleration and etc.) of an object moving in space by simulation. For the algorithm proposed in this thesis, outputs of 6 linear accelerometers were employed in the state equation and outputs of the other redundant linear accelerometers were used for the output equation; furthermore, Iterated Extended Kalman filter was treated as a nonlinear observer in order to stabilize the nonlinear dynamic equation and estimate precise state (angular rate in the rotation frame). Euler's transform is employed to transfer the physical quantities from the basis of rotation frame to the inertial frame. The result (angular rate in the inertial frame) from algorithm undergoes single integration to obtain 3 rotation angles; and result (linear acceleration in the inertial frame) undergoes double integration to obtain 3 coordinates for location.

Because Euler's angular displacement is obtained from solving differential equation (2.37), this integral operation would accumulate the error and make serious mistake by using Euler's transform. Algorithm flow (Fig.4.1.2) indicated that the influence of the error due to integration (Euler's angle) on linear acceleration in the inertial frame is the most serious. For the linear acceleration in the rotation frame obtained by (4.6) carries about a lot of white noise, it must be incorrect when we transfer it into linear acceleration in the inertial frame with Euler's transformation. The same problem would come out while transferring the angular rate from that on the basis of rotation frame to inertial frame.

It has to be mentioned that the angular rate in the rotation frame is obtained by Kalman filter without white noise, and it is more accurate than the linear acceleration.

Some experimental errors would cause the difference between encoder information and outputs/states of the algorithm. In this thesis, we pointed out that linear vibration affects linear acceleration, rotational vibration affects angular rate respectively, and DC-drift or other noises affect the convergent rate more seriously than the vibrations we discuss above.

5.2 Future works

Although the preliminary simulation/experiment of observer-base planar Gyro-Free IMU is proposed in this work, more complete simulation, experiment and fabrication have to be done in the future, as listed below:

1. To implement observer-base planar Gyro-Free IMU with control circuitry by MEMS process.
2. To improve the resolution for further reducing the restrictions on the distance between accelerometers and origin point in the rotation frame.
3. Replace Euler's angle by Euler's parameters in order to reduce the accumulation of error due to integration.
4. To complete the 6-axes experiment and reduce experimental error.

References

- [1] **A. J. Padgaonkar and K. W. Krieger and A. I. King,**” Measurement of Angular Acceleration of Rigid Body Using Linear Accelerometers”, *Journal of applied Mechanics, Transactions of the American Society of Mechanical Engineers*, Vol.42, pp.552-556, September 1975
- [2] **Jeng-Heng Chen and Sou-Chen Lee and Daniel B. DeBra,**” Gyroscope Free Strapdown Inertial Measurement Unit by Six Linear Accelerometers”, *Journal of Guidance, Control and Dynamics*, Vol.17, No.2, March-April 1994
- [3] **A. R. Schuler and A. Grammatikos and K. A. Fegley,** “Measuring Rotational Motion with Linear Accelerometers”, *IEEE Transactions on Aerospace and Electronic Systems*, Vol. AES-3, No.3, pp.465-471, May 1967
- [4] **T. R. Kane and P. W. Linkins and D. A. Levinson,** *Spacecraft Dynamics*, McGraw-Hill, 1983
- [5] **P. C. Hughes,** *Spacecraft Attitude Dynamics*, Wiley, 1986
- [6] **F. F. Ling,** *Introductory Attitude Dynamics*, Springer-Verlag, 1988
- [7] **H. Goldstein and C. Poole and J. Safko,** *Classical Mechanics*, Addison Wesley, 2001
- [8] **Alberto Leon-Garcia,** *Probability and Random Processes for Electrical Engineering*, Addison Wesley, 1994
- [9] **A. Papoulis,** *Probability Random Variables and Stochastic Processes*, McGraw-Hill, 1991
- [10] **Yaakov Bar-Shalom and X.-Rong Li and Thiagalingam Kirubarajan,** *Estimation with Applications To Tracking and Navigation*, Wiley, 2001
- [11] **謝銘峰,** *GPS/DGPS 與慣性導航系統之整合研究*, 國立交通大學控制工程研究
- [12] **黃國興,** *慣性導航系統原理與應用*, 全華科技圖書股份有限公司, 中華民國 80 年